Chapter 5. Experimental Diagnostics

5.0 INTRODUCTION

The Omega Facility can field a comprehensive suite of diagnostics for a variety of high-energy-density physics experiments. This chapter documents charged-particle and nuclear diagnostics (Secs. 5.1 and 5.2, respectively); x-ray diagnostics (Secs. 5.3–5.7); optical diagnostics (Secs. 5.8–5.13); magnetic field diagnostics (Sec. 5.14); and diagnostic systems developed by external users of the Omega Facility (Sec. 5.15).

5.1 CHARGED-PARTICLE DIAGNOSTICS

5.1.1 Nuclear Reactions Producing Charged Particles and Energetic Neutrons

Nuclear reactions in the fusion fuel produce energetic neutrons and a variety of charged particles including p, D, T, and ^{4}He. The primary diagnostics used at the Omega Facility to measure these charged particles include magnet-based charged-particle spectrometers and the proton-temporal diagnostics.

Charged particles and energetic neutrons arise from a number of nuclear reactions:

(a) *Primary Reactions from DT Fuel*

$$\mathrm{D} + \mathrm{T} \rightarrow {}^4\mathrm{He}(3.5\ \mathrm{MeV}) + \mathrm{n}(14.1\ \mathrm{MeV}). \tag{5.1.1}$$

The 14.1-MeV neutron yield is routinely measured using copper activation and scintillator-based detectors (Secs. 5.2.1 and 5.2.2). Alpha particles (^{4}He^{++}) undergo substantial energy loss in the compressed plastic shells of typical non-cryogenic OMEGA targets and, therefore, cannot routinely be used as a diagnostic. For very thin shells, the alpha particles escape with little energy loss since the areal densities are very small (~1 mg/cm^2). In this case, a cross-calibration has been made directly between the neutron detectors and the charged-particle spectrometers using the implosion of thin glass-shell targets filled with DT.[1]

A second branch of the D–T reaction emits a 16.7-MeV gamma ray,[2] with a branching ratio of $<10^{-4}$:

$$\mathrm{D} + \mathrm{T} \rightarrow {}^5\mathrm{He} + \gamma(16.7\ \mathrm{MeV}). \tag{5.1.2}$$

The gammas are produced via the decay of ^{5}He from an excited state to a ground state. The gammas recorded via the Cherenkov processes in external-user–developed diagnostics (Sec. 5.15).

(b) *Primary Reactions from D_2 Fuel*

In D_2 fuel, the primary nuclear reactions comprise two branches with approximately equal probabilities:

$$\mathrm{D+D}\begin{cases}{}^3\mathrm{He}(0.82\ \mathrm{MeV})+\mathrm{n}(2.45\ \mathrm{MeV}) \quad (\sim 50\%) & (5.1.3a)\\ \mathrm{T}(1.05\ \mathrm{MeV})+\mathrm{p}(3.02\ \mathrm{MeV}) \quad (\sim 50\%)\,. & (5.1.3b)\end{cases}$$

Indium activation detectors (Sec. 5.2.1) and scintillator-based detectors (Sec. 5.2.2) are used to diagnose the neutron yield of D_2 implosions.

(c) *Secondary Reactions from D_2 Fuel*

The ^{3}He and triton products from the above two reactions [Eq. (5.1.3)] can combine with fuel deuterium in the following "secondary" reactions:

$$\mathrm{T}^* + \mathrm{D} \rightarrow {}^4\mathrm{He} + \mathrm{n}(11.8 - 17.1\ \mathrm{MeV}) \quad (5.1.4a)$$

$$^3\mathrm{He}^* + \mathrm{D} \rightarrow {}^4\mathrm{He} + \mathrm{p}(12.5 - 17.4\ \mathrm{MeV}), \quad (5.1.4b)$$

where T* and ^{3}He* indicate tritons and ^{3}He nuclei that can have energies less than their corresponding birth energies [Eq. (5.1.3)] because of slowing down in the target.

With models of the fuel region, neutron and proton yields from these reactions can be used to estimate the fuel areal density $(\rho R)_{\mathrm{F}}$ (Refs. 3–8). The estimated value depends on the model used. For example, the $(\rho R)_{\mathrm{F}}$ obtained from an "ice-block" model (a uniform fuel and source) is ~34% larger than that obtained from a hot-spot model (a point source surrounded by uniform fuel).[3] *LILAC* simulations suggest that the ice-block model is more appropriate for current OMEGA experiments.

Information about the shell areal density can be inferred from the proton spectra. The downshift of the energetic protons [Eq. (5.1.4b)] is relatively insensitive to temperature (for gas-filled and cryogenic targets on OMEGA) and depends primarily on the shell areal density.[3] Secondary proton spectra measured using the charged-particle spectrometers (Sec. 5.1.2) and the wedge-range-filter proton spectrometers (Sec. 5.1.3) have been used to provide information about the shell areal density.[3]

(d) *Knock-On Reactions in DT-Filled Targets*

Up-scattered DT fuel nuclei ("knock-ons"[9]) and knock-on protons from the shell[10] are produced in the following reactions:

$$\mathrm{n} + \mathrm{D} \rightarrow \mathrm{n}' + \mathrm{D}'(0 - 12.5\ \mathrm{MeV}) \quad (5.1.5a)$$

$$\mathrm{n} + \mathrm{T} \rightarrow \mathrm{n}' + \mathrm{T}'(0 - 10.5\,\mathrm{MeV}) \tag{5.1.5b}$$

$$\mathrm{n} + \mathrm{p} \rightarrow \mathrm{n}' + \mathrm{p}'(0 - 14.1\,\mathrm{MeV}), \tag{5.1.5c}$$

where n indicates the 14.1-MeV neutron from the D–T reaction and T′, D′, and p′ indicate tritons, deuterons, and protons, respectively, at energies in the ranges shown in parentheses. Triton and deuteron spectra measured using the charged-particle spectrometers[11] (Sec. 5.1.2) have been used to identify the target fuel and shell areal densities. The number of each of these particles in the high-energy peak in the spectrum is proportional to the fuel areal density, and the downshift of this peak provides a measure of the shell areal density.[9,11,12]

For areal densities $\rho R \lesssim 100$ mg/cm^2, the proton knock-on yield in a suitably chosen energy range (10.5 to 12.0 MeV) is proportional to the areal density of the shell.[13] Proton knock-on spectra have been measured using the charged-particle spectrometers and wedge-range-filter proton spectrometers (Sec. 5.1.3).[11,12,14]

The number of elastically scattered neutrons ("down-scattered" neutrons) is proportional to ρR and is relatively independent of the details of the density profile. The down-scattered spectrum is used to infer the areal density in cryogenic DT implosions on both OMEGA and the NIF using the magnetic recoil spectrometer (Sec. 5.2.5) and scintillator-based neutron time-of-flight detectors (Sec. 5.2.2).

(e) *Tertiary Reactions from DT Fuel*

"Knock-on" tritons and deuterons can further interact with thermal DT fuel nuclei, producing the "tertiary" reactions:[15–17]

$$\mathrm{D}' + \mathrm{T} \rightarrow {}^4\mathrm{He} + \mathrm{n}(12 - 30.0\,\mathrm{MeV}), \tag{5.1.6a}$$

$$\mathrm{T}' + \mathrm{D}' \rightarrow {}^4\mathrm{He} + \mathrm{n}(9.2 - 28.3\,\mathrm{MeV}), \tag{5.1.6b}$$

where D′ and T′ indicate the knock-on particles.

Tertiary reactions are expected to be an important diagnostic for NIF implosions because of the high expected fuel areal densities.

(f) *Primary Reactions from D^{3}He Fuel*

Primary nuclear reactions from D^{3}He fuel comprise the primary D–D reactions [Eq. (2.5.3)] plus the following reaction:

$$\mathrm{D} + {}^3\mathrm{He} \rightarrow {}^4\mathrm{He}(3.6\,\mathrm{MeV}) + \mathrm{p}(14.7\,\mathrm{MeV}). \tag{5.1.7}$$

Similar to the secondary protons, the downshift of the primary D–^{3}He protons[18] is proportional to the total areal density of the compressed target. Being relatively insensitive to temperature for the areal densities of interest in OMEGA implosions, this diagnostic has been successfully used to infer compressed-shell areal densities in D^{3}Hefilled targets.[12,19–21] The range of these protons limits this diagnostic to values of areal density up to ~300 mg/cm^2 (Refs. 18 and 19).

The neutron-averaged temperature of the fuel ions can be estimated from the ratio of D–D neutrons [Eq. (2.5.3a)] to D–^{3}He protons.[19]

(g) *Secondary Reactions from D^{3}He Fuel*

In addition to the D–D secondary reactions of Eq. (2.5.4), the following secondary reactions can occur in D–^{3}He-filled targets:

$$T^{*} + {}^{3}\mathrm{He} \rightarrow \begin{cases} {}^{4}\mathrm{He} + \mathrm{p} + \mathrm{n}(12.1\ \mathrm{MeV}) & (\sim 51\%) \\ {}^{4}\mathrm{He}(4.8\ \mathrm{MeV}) + \mathrm{D}(9.5\ \mathrm{MeV}) & (\sim 43\%) \\ {}^{5}\mathrm{He}(2.4\ \mathrm{MeV}) + \mathrm{p}(11.9\ \mathrm{MeV}) & (\sim 6\%). \end{cases} \tag{5.1.8}$$

With their very low reaction rates, the T–^{3}He reactions provide observable signals only in special circumstances. For example, the implosion of a thin, T^{3}He-filled glass shell can reach very high temperatures, leading to an observable signal for the 9.5-MeV deuterons. In this case, because of the relatively low areal densities, the emergent deuterons are relatively monoenergetic and consequently have been used to calibrate the two charged-particle spectrometers.

5.1.2 Magnet-Based Charged-Particle Spectrometers

Two charged-particle spectrometers (CPS's) on OMEGA can measure the spectra of several particle species (e.g., p, D, T, ^{3}He, ^{4}He) simultaneously. They use 7.6-kG permanent magnets for energy discrimination and CR-39 for particle detection (see Refs. 1, 22, and 23 for detailed descriptions of these instruments). The design of the magnet and the system geometry makes possible the study of a very wide range of particle energies (0.1 to 30 MeV for protons), while the CR-39 detectors count individual particles and provide discrimination among different particle types. The dynamic range of a CPS is determined by the size of the entrance aperture, the distance from the target, and the minimum and maximum number of particles per unit area that can be measured with CR-39; particle yields from ~10^7 per MeV to at least 10^{16} per MeV can be accommodated. The energy resolution is better than 4% and the absolute energy calibration is better than 0.1 MeV.

The range of particle types, energies, and yields covered by a CPS has made possible the study of many types of implosions. Of particular importance are (1) knock-on D and T spectra from room-temperature and cryogenic DT-filled targets, allowing the study of fuel areal density;[10]

(2) knock-on proton spectra from DT-filled CH targets for the study of shell areal density;[11] and (3) D^3He and DD protons from D^3He-filled targets for the study of shell areal density.[19] The fact that there are two CPS's viewing the implosion from different directions makes possible rudimentary symmetry measurements.

5.1.3 Wedge-Range-Filter Proton Spectrometers

A second type of spectrometer, known as the wedge-range-filter (WRF) spectrometer, was developed specifically for the study of protons.[1,22,24] This simple and compact spectrometer uses a CR-39 detector, which records the tracks of individual particles and has energy discrimination for protons in the range of 0.5 to 8 MeV, behind a filter whose thickness varies with position (with a wedge-shaped cross section). The energy of each detected particle is measured, and the thickness of the filter it passed through is used to calculate the energy the particle had before it encountered the filter. Theoretically, a filter with an appropriate range of thicknesses could be used to find the spectra of protons from 0.5 MeV up to an arbitrarily high energy. The first-generation WRF spectrometers, deployed in 2001, used Al filters with thickness varying from 400 to 1800 μm to provide coverage of proton energies from 8 to 18 MeV.

Unlike the CPS's, these spectrometers cannot measure spectra of different particle species simultaneously and cannot cover a large energy range. However, they can measure proton spectra at much lower yields than the CPS's (by more than two orders of magnitude) and at many different angles simultaneously. As a result, they have allowed several important areas of study. Their high sensitivity has made possible the accurate measurement of secondary D^3He protons from D_2-filled targets, which generally have yields lower than the CPS limit. This has led to the WRF spectrometer becoming the standard instrument for the study of shell areal density for D_2-filled targets (Ref. 24). The high sensitivity allows the measurement of primary D^3He-proton spectra in cases where the yield is low (e.g., in mix experiments involving a pure ^3He fill in shells having CD sublayers[25] and in indirect-drive experiments using D^3He-filled targets[26]). The fact that many WRF spectrometers can be deployed simultaneously has made possible many studies of areal density symmetry with D_2-filled targets,[24] D^3He-filled targets,[10,27–30] and DT-filled targets.[26]

5.1.4 High-Areal-Density Wedge-Range-Flter Spectrometers

The 8- to 18-MeV energy range of the original WRF spectrometers proved to be satisfactory until recently, when low-adiabat experiments with D_2-filled targets and thick CH shells began to result in areal densities high enough to require a low-energy measurement limit well below 8 MeV. For several years it has been anticipated that the areal densities of cryogenic D_2 targets would approach 200 mg/cm^2 and result in secondary proton energies as low as 3 MeV.

As a consequence, a new WRF design has been developed utilizing a wedge filter that expands the energy coverage from 3 to 25 MeV. The material used for the filter is zirconia, with a thickness varying from 15 μm to 1600 μm (used in conjunction with a 25-μm Al blast shield). Twenty five of these have been fabricated, and they have performed well.

5.1.5 Proton Temporal Diagnostic

A proton temporal diagnostic (PTD) was developed to record the fusion reaction rate history of protons generated from the thermonuclear burn of D^3He- and D_2-fueled targets on OMEGA.[28] The primary purpose of the PTD is to measure the temporal history of primary D^3He protons generated via Eq. (5.1.7) with an energy of 14.7 MeV. The PTD is also sensitive to secondary protons (12.6 to 17.5 MeV) and primary neutrons (2.45 MeV) from D_2-fueled targets, according to Eqs. [2.5.4(b)] and [2.5.3(a)], respectively.

The PTD detector system, shown schematically in Fig. 5.1, was developed as a modification of the existing OMEGA neutron temporal diagnostic—the cryoNTD.[29] The PTD was designed to operate in one of the OMEGA ten-inch manipulators (TIM's). It is based on a fast scintillator (BC-422) that acts as a proton-to-light converter shielded by two thin (100- to 200-μm) Al and Ta foils against x-ray and direct laser illumination. An optical system, including 11 lenses and 2 mirrors,[29] transfers the scintillator light through the TIM and the vacuum window along a 3.5-m optical path to a high-speed optical streak camera.[30] The front end of the optical system is mounted in the TIM and inserted close to the target. Since the PTD uses the existing cryoNTD optics and mechanical assembly, the PTD scintillator is located 9 cm from the target, the required standoff distance for OMEGA cryogenic target operations. With additional optics, the PTD scintillator can be placed closer to noncryogenic targets to improve the temporal resolution. A simultaneously recorded optical fiducial provides a reference for accurate timing with respect to the incident laser pulse.

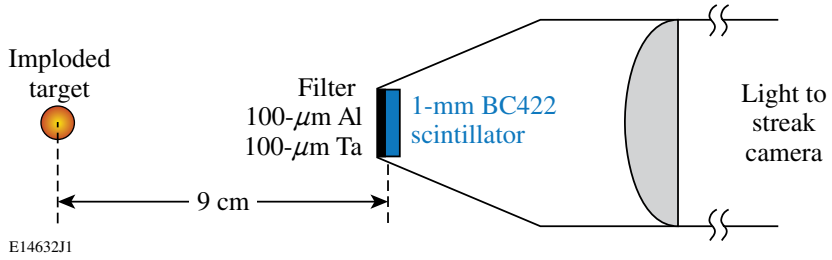

Figure 5.1
Schematic of the proton temporal diagnostic (PTD) detector system on OMEGA. The detector is based on a fast scintillator that acts as a proton-to-light converter protected by Al and Ta foils against x-ray and direct laser illumination. An optical system transfers the scintillator light to a streak camera.

Figure 5.2(a) shows a sample image, recorded by a charge-coupled–device (CCD) camera attached to the streak camera, for a D^3He implosion with a proton yield of 5.7×10^7. The fiducial train is at the top of the image and the scintillator output is in the center. After the PTD signal is averaged across the central portion of the scintillator, the streak-camera flat-field and geometric distortions are removed and the CCD background from the bottom portion of the image is subtracted to create the final temporal trace [Fig. 5.2(b)]. This trace has three distinct components: an early x-ray peak resulting from hard x rays[31] of energy >30 keV, presumed to originate via bremsstrahlung from suprathermal electrons created by the two-plasmon instability in the target corona, and the shock and

compression proton peaks. In contrast to the NTD, where the neutron yield at shock convergence is ~100 times smaller than the yield at peak compression, the shock and compression proton peaks of the PTD are comparable for D^3He implosions (because of the stronger temperature dependence of the proton-production cross section).

The BC-422 scintillator has a very fast rise time (<20 ps) and a decay time of ~1.2 ns, as seen in the x-ray peak of Fig. 5.2(b). The scintillator decay from x rays creates a background for the proton signal. Since it is difficult to calculate this background level, the filter thickness was optimized experimentally. The PTD background depends on many parameters such as the laser energy, pulse shape, and target design. The filter-thickness optimization required a series of identical shots where all parameters except the filter thickness were fixed.

The nose cone is the main difference between the PTD and the cryoNTD.[32] The design of the PTD nose cone satisfies several criteria: (1) it is light tight to prevent direct laser illumination; (2) it survives ablation, target debris, and the thermal impulse from the target implosion; (3) it is

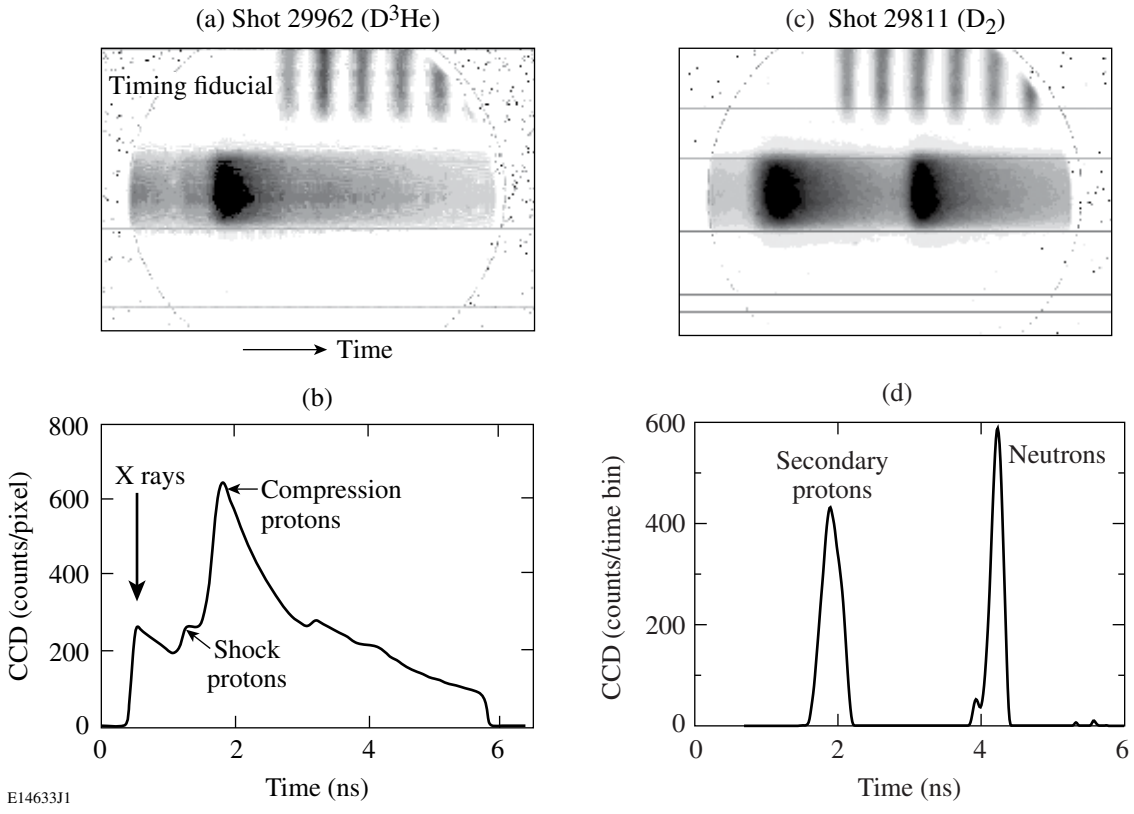

Figure 5.2
(a) The PTD streak camera image from shot 29962, in which a 24-μm-thick plastic shell filled with 18 atm of D^3He was imploded on OMEGA with a 1-ns pulse shape and 23 kJ of energy. (b) The PTD signal averaged across the central portion of the scintillator with the CCD background subtracted and with the streak-camera flat-field and geometric distortions taken into account. (c) Same as (a) but for shot 29811, in which a 20-μm-thick plastic shell was filled with 15 atm of D_2. (d) Same as (b) but for shot 29811 and with correction made for the 1.2-ns scintillator decay time.

transparent to protons with energies larger than 10 MeV; and (4) it absorbs as much of the soft-x-ray radiation as possible. Tantalum was chosen as the PTD filter material because of its strength and hardness and because 25-mm-diam tantalum foil disks are commercially available.[33] An additional 100-μm Al filter placed in front of the Ta foil reduces a spurious PTD signal caused by hard x rays generated from suprathermal electrons hitting the foil; this filter reduces the hard-x-ray background by a factor of 4, while the proton signal is reduced only 10% to 20% depending on the proton energy. A 0.3-mm-thick plastic spacer ring is inserted between the filter foils and the scintillator to prevent the scintillator from melting due to the heating of the filters by light, x rays, and plasma from the target. It is possible to change the PTD nose cone to the cryoNTD nose cone or to change the PTD filter-foil/scintillator combination within the 45-min OMEGA shot cycle. Tests done with 100-μm Ta foils placed 9 cm from the target show that these foils survive more than 50 direct-drive OMEGA shots without damage.

Absolute timing is established using the OMEGA fiducial system. The OMEGA fiducial beam consists of a series of eight 0.53-μm pulses spaced 548 ps apart and is synchronized to the OMEGA laser pulse with a jitter of less than 20 ps. The optical fiducial is amplified separately from the main laser pulse, split, and distributed to various diagnostic instruments for precision timing. The fiducial pulse train is recorded on the P510 ultraviolet streak cameras[32] that are used to record the laser pulse shapes for each of OMEGA's 60 beams. The common optical fiducial serves as a reference for both the proton signal and the laser pulse, enabling very accurate timing of PTD signals relative to the laser pulse. The recorded fiducial pulse [Fig. 5.2(a)] is fit by a train of eight Gaussian pulses spaced at a well-characterized period of 548 ps (Ref. 32). This reduces the influence of noise on the determination of the timing reference.

The PTD is designed for multiple fusion-reaction products and multiple standoff distances. Its fiducial has ten delay fibers with nominal delays from 1 ns to 10 ns in steps of 1 ns. These fibers were characterized at the Lawrence Livermore National Laboratory with an accuracy of better than 3 ps using 45-ps-FWHM, 0.53-μm laser pulses (the same wavelength as the OMEGA fiducial). The PTD streak camera has 3#, 5#, and 10# sweep cards that create approximately 3-ns, 5-ns, and 10-ns time windows with pixel resolutions of 7.5 ps, 13 ps, and 23 ps, respectively.

While the PTD is primarily intended for use with D^3He implosions, it is also used for D_2 implosions. A typical PTD streak camera image for a D_2 implosion with a neutron yield of 1.3×10^{11} is shown in Fig. 5.2(c) with its deconvolved signal in Fig. 5.2(d). In a D_2 implosion, the first PTD peak is the signal from secondary protons with energies of 12.6 to 17.5 MeV and the second peak is the signal from the 2.45-MeV DD neutrons. (The structure near the start of the neutron signal indicates shock-produced neutrons.) Although the yields of secondary protons and primary neutrons differ by a factor of 1000, the PTD signals are comparable due to the different interaction mechanisms of protons and neutrons within the scintillator.

The PTD neutron signal from a D_2 implosion is used to determine the time of peak neutron production (the bang time) similar to the NTD.[34] The bang times measured by the two instruments correlate to ~30 ps (rms).

The secondary-proton peak in the PTD signal seen in Fig. 5.2(d) is used to measure the secondary-proton yield in D_2 implosions above 1×10^7. The average energy downshift of these protons is routinely used on OMEGA to measure the total areal density of the target[20] (see also Sec. 5.1.3). The average energy downshift of the secondary protons is inferred from the PTD, based on the time-of-flight difference between the secondary-proton and the primary-neutron peaks. From the secondary proton's energy downshift, the total areal density can be calculated by using plasma-stopping formulas[35] as with wedge-range-filter spectrometer data (Sec. 5.1.3). A comparison with the total-areal-density data inferred from the charged-particle spectrometers shows significant differences,[36] probably due to known areal-density asymmetries[24] on OMEGA.

Protons emitted from the D^3He reaction lose energy when passing through the compressed capsule shell. The areal density of target material through which the protons pass determines the amount of energy loss. Therefore, by measuring the proton-production history with the PTD and simultaneously a time-integrated proton-energy spectrum by charged-particle spectroscopy, the temporal evolution of the target areal density can be inferred. The areal-density evolution in D^3He implosions was first studied in Ref. 36 with the assumption that the D^3He proton-production history is proportional to the D_2 neutron-production history. With the development of the PTD, the areal density evolution can now be inferred using the proton-production history.[28]

Further information on the PTD can be found in Ref. 36.

5.1.6 Ultrafast Proton Radiography

High-energy petawatt lasers accelerate protons in thin-foil target interactions.[37] Substantial proton fluxes up to several tens of MeV have been demonstrated with OMEGA EP using kJ-class, 1- to 10-ps pulses focused to intensities of more than 10^{18} W/cm^2 (Ref. 38). These protons have high brilliance, small source size, and are highly collimated—properties ideal for radiographic applications.[39] In addition to providing information on areal density variations inside solid and laser-compressed matter, they can detect highly transient electric and magnetic fields.

The proton source derives from water and hydrocarbon contaminants on the surface of thin-foil targets. At laser intensities above 10^{18} W/cm^2, hot electrons are accelerated at the target front surface and propagate through the target, exiting through the rear surface. The plasma sheath that forms supports electric fields of up to 10^{12} V/m. These fields ionize the target surface and accelerate protons to MeV energies by the target normal sheath acceleration (TNSA) mechanism.[37]

On OMEGA EP, the proton source typically contains $>10^{12}$ protons with energies above 3 MeV. The energy spectrum of the source is broad and has temperatures in the MeV range. Proton energies typically extend to several tens of MeV. The source is highly directional and has a small angular aperture at the highest proton energies. While the protons are accelerated from an extended region over the target-rear surface, the sheath-field topology maintains a highly laminar source. This is important for proton radiography applications because it allows for micron-scale spatial resolution from a virtual point source.

A typical proton radiography setup includes a proton-source foil, a radiography object, and a radiochromic film (RCF) detector stack.[40] A high-intensity laser pulse irradiates the proton-source foil a distance L_1 from the radiography object, and a distance $(L_1 + L_2)$ from the RCF detector. The image magnification is $M \approx (L_1 + L_2)/L_1$. Protons propagate across the radiography object and are scattered or stopped as they travel through the target material. Electromagnetic fields generated by a laser-driven radiography object deflect the proton trajectories and contribute to modulating the proton-beam profile before it is measured.

The proton beam is measured with an RCF detector stack. The stack typically contains >10 pieces of RCF and is filtered with aluminum foils to detect the entire proton-energy spectrum. Protons deposit their energy within the detector stack at a depth given by the Bragg peak, which varies as a function of proton energy. The protons have subrelativistic velocities, and time-of-flight dispersion provides a unique spectral and temporal, multiframe imaging capability. On a single-shot, multiple point-projection images are measured at different times with picosecond-scale resolution. The time between frames is geometry dependent and typically varies from several to tens of picoseconds. This allows for the study of highly transient electromagnetic and hydrodynamic phenomena in solid and laser-compressed matter.

Figure 5.3 shows measurements of the proton source size for thin-foil target experiments carried out on OMEGA EP. Figure 5.3(a) shows a schematic of the proton-source foil and indicates how the curved rear-surface sheath field generates a virtual point source that is much smaller than the laser focal spot. The source size was measured by imprinting the image of a wire mesh on the proton-beam profile. The mesh contains 26-μm wires separated by 35-μm holes. The source size is defined by edge-resolution measurements across the field of view. Figure 5.3(b) shows an example of an edge-resolution measurement for 5-MeV protons, demonstrating few-micron spatial resolution. Over the entire field of view, the average spatial resolution is 4±2 μm. Mesh-imprint distortion can also

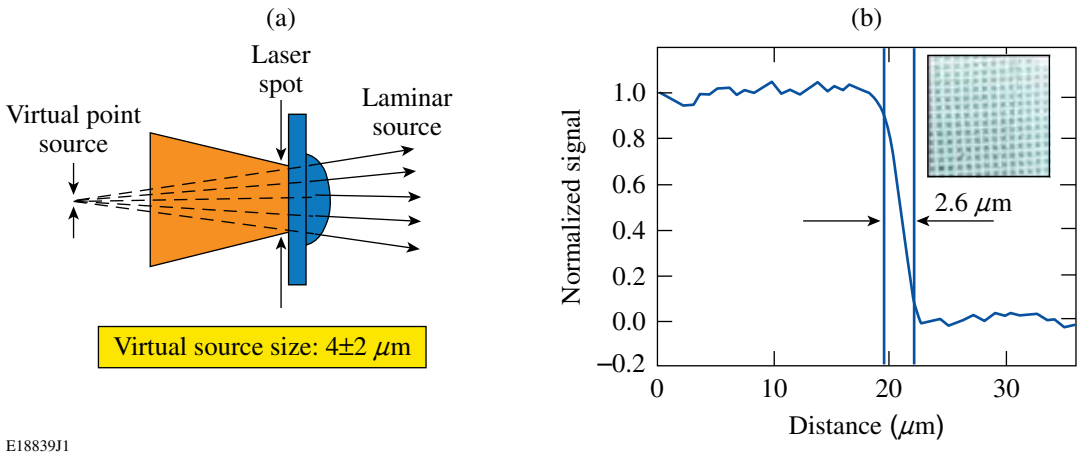

Figure 5.3
(a) Schematic of a virtual point source generated in laser-driven proton radiography. (b) Proton source-size measurements for 5-MeV protons backlighting a wire mesh.

provide a metric for how far the proton beam is deflected across an image plane by electromagnetic fields in a driven target. The magnitude of these fields can be determined from the mesh distortion by careful choice of target geometry.

5.2 NEUTRON DIAGNOSTICS

A large suite of neutron diagnostic systems are operational on OMEGA to routinely diagnose spherical implosion experiments. They are listed in Table 5.1 with the parameters that they measure and their ranges of applicability.

Table 5.1: Neutron diagnostics for the OMEGA laser. (PMT: photomultiplier tube; MCP: microchannel plate; CVD: chemical vapor deposition; NTD: neutron temporal diagnostic; NBT: neutron bang time; HYNBT: high-yield NBT.)

Measured Parameter	Instrument	Applicable Yield Range
Neutron yield	Cu activation In activation Scintillator/PMT	$1 \times 10^8 < Y < 1 \times 10^{16}$ (DT) $1 \times 10^9 < Y < 1 \times 10^{12}$ (DD) $5 \times 10^4 < Y < 1 \times 10^{15}$
Fuel areal density	Secondary yield (scintillator/PMT)	$5 \times 10^5 < Y < 1 \times 10^{11}$
Fuel ion temperature	Scintillators/(MCP-PMT) and CVD diamond detectors	$Y > 2 \times 10^8$ (DD) $Y > 1 \times 10^9$ (DT)
Neutron-emission time history	Scintillator/streak camera (NTD)	$1 \times 10^9 < Y < 3 \times 10^{13}$
Neutron bang time	Scintillator/PMT (NBT) CVD diamonds (HYNBT)	$1 \times 10^7 < Y < 1 \times 10^{11}$ $5 \times 10^{10} < Y < 1 \times 10^{15}$

The primary neutron yield is measured by two sets of diagnostics, one based on copper and indium nuclear activation and the other using current-mode neutron time-of-flight (nTOF) detectors. The yield range of these diagnostics covers ten orders of magnitude. The secondary neutron yield is measured using copper activation and scintillator/photomultiplier nTOF detectors.[8] Some of the nTOF detectors have sufficient sensitivity and temporal resolution to determine the burn-averaged ion temperature.

The neutron burn history of both room-temperature targets and cryogenic DT targets is measured on OMEGA with the neutron temporal diagnostic (NTD).[13] The neutron burn history of cryogenic D_2 targets is measured with the "cryoNTD"[29] located in a ten-inch-manipulator. A neutron bang-time detector (NBT)[41] determines the time of peak neutron production for shots with low neutron yields. A high-yield neutron bang-time detector (HYNBT)[42] is used to measure the bang time for high-yield shots.

5.2.1 Activation Detectors

The activation systems include copper activation [^{63}Cu(n,2n)^{62}Cu with a 10.9-MeV threshold and a decay by positron emission] to detect 14.1-MeV neutrons from DT fuel experiments and indium activation [^{115}In(n,n′)^{115m}In, with a 330-keV threshold and a decay with the emission of a 336.2-keV gamma ray] to detect 2.45-MeV neutrons from D_2 fuel. Before a shot, the Cu activation sample is manually placed in a pneumatic retractor holder and inserted into the target chamber 40 cm from the target. Immediately after the shot, the activated sample is retracted from the chamber and dropped via

a plastic tube to a pickup basket in a room under the Target Bay. The operator picks up the activated Cu sample from the basket and delivers it to a counting room. The time from the shot to the start of counting is 3 to 5 min. The indium activation sample is manually inserted and retracted using a ten-inch-manipulator port. The indium sample is located at 9.4 cm from the target. Two different systems are used to count the activation samples.

The positrons resulting from copper activation are detected using an NaI coincidence system, consisting of two 7.6-cm × 7.6-cm NaI(Tl) detectors and associated electronics. This system measures coincident 511-keV gamma rays from positron annihilation. Using copper disks of different mass, the copper activation diagnostic can measure neutron yields from DT-filled targets from 1×10^8 to 1×10^{16}.

The activation of the indium samples is detected with a high-resolution gamma-ray spectrometer that uses a high-purity-germanium (HPGe) detector. The indium activation measures the neutron yield from 1×10^9 to 1×10^{12}.

Both the indium and the copper activation systems have been absolutely calibrated using several methods. All agree within 10%, determining the error in the absolute yield. The relative shot-to-shot error for activation systems is dominated by the counting statistics and is below 3% for high-yield shots.

5.2.2 Neutron Time-of-Flight Detectors

Several current-mode scintillator/photomultiplier-based detectors or chemical-vapor-deposition (CVD) diamond detectors[43–45] with overlapping, staggered sensitivities measure the full range (ten orders of magnitude) of primary and secondary neutron yields on OMEGA. Some detectors can measure both the primary and secondary yields, while others can measure only the primary yield. They complement the activation diagnostics. The scintillator yield measurements are calibrated *in situ* by comparison with the activation systems for both 2.45-MeV and 14.1-MeV neutrons.

The scintillators have various volumes and are mounted at various distances from the target. Each detector is shielded from prompt x-ray and *n*–c radiation by lead that varies in thickness between detectors from 1.27 cm to 5 cm. Two CVD diamond detectors have 10-mm-diam, 1-mm-thick CVD wafers and are located at 2.8 and 5.3 m from the target. The signal from each detector is split and recorded on two channels of a 1-GHz, 5-GS/s Tektronix TDS-684 digital oscilloscope.[46] For all target shots, PC-based data-acquisition programs record the data from the oscilloscopes. An on-line program analyzes this data and makes the results available about 10 min after the shot.

Several of the scintillator/photomultiplier-based detectors can measure the thermal broadening of the neutron signal, enabling an ion-temperature measurement.[47] They use fast microchannel-plate photomultiplier tubes (MCP-PMT's) coupled to quenched plastic scintillators. Two CVD diamond detectors are also used for ion-temperature measurements at high DT yields. The time-of-flight signals are fit up to their trailing half-maximum to exclude the contribution at later times due to c rays from *n*–c reactions.

The upgraded 13.4-m line-of-sight can measure the entire neutron-energy spectrum from 1 to 16 MeV. The signal-to-background ratio can be improved by the introduction of a mid-beam collimator. A diagram of the setup of the current nTOF detector and mid-beam collimator is shown in Fig. 5.4.

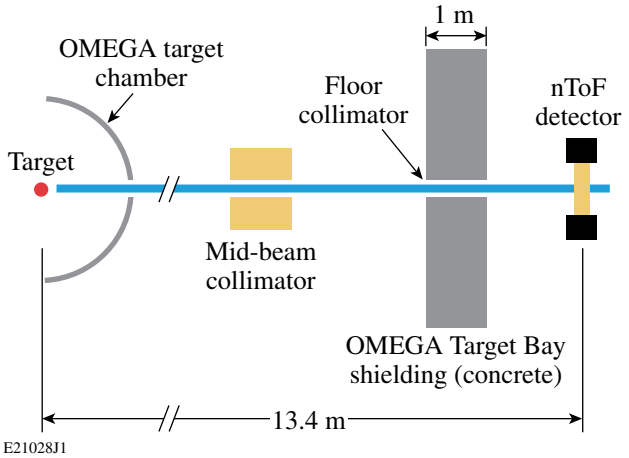

Figure 5.4
A schematic of the setup of the nTOF diagnostics shows the concrete shielding, the nTOF detector clear line of sight, and the mid-beam collimator. It was determined that the primary DT neutrons scatter off the target chamber walls and produce a large background signal in the nTOF.

The mid-beam collimator has a 60-cm-sq cross section and is ~70 cm in length. It is constructed from high-density polyethylene with a density of ~0.95 g/cm^3. It is mounted on a stand located in the OMEGA Target Bay with permanent static mounts.

The neutron time-of-flight (nTOF) detector has a cylindrical thin-wall stainless-steel, 8-in.-diam, 4-in.-thick cavity filled with an oxygenated xylene scintillator (Fig. 5.5). Four gated photomultiplier tubes (PMT's) with different gains are used to measure primary DT and D_2 neutrons, down-scattered neutrons in nT- and nD-edge regions, and tertiary neutrons in the same detector (Fig. 5.6). The nTOF detector is located 13.4 m from the target chamber center in a collimated line of sight.

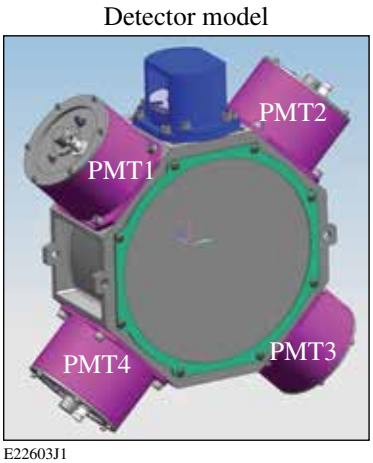

Figure 5.5
A schematic of a nTOF detector with four gated photomultiplier tubes (PMT's).

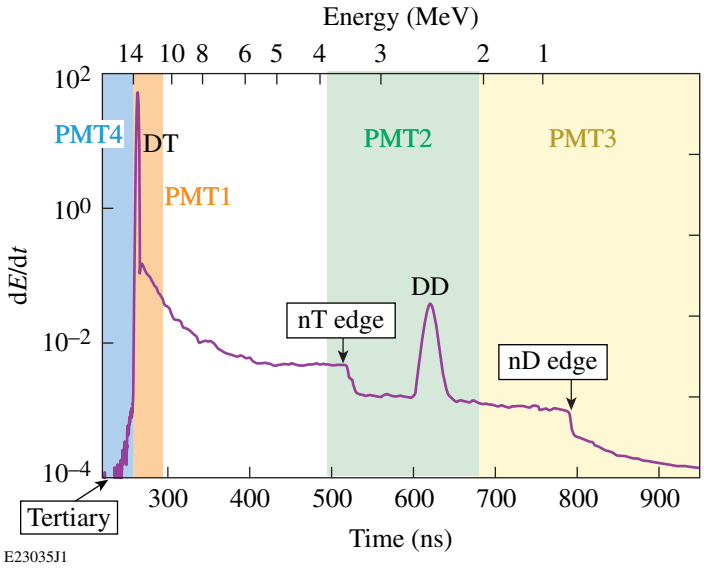

Figure 5.6
Graph illustrating the neutron spectrum measurement capability of the nTOF detector.

The areal density (ρR) of cryogenic DT implosions on OMEGA is inferred by measuring the spectrum of neutrons that elastically scatter off the dense deuterium (D) and tritium (T) fuel. Neutron time-of-flight (nTOF) techniques are used to measure the energy spectrum with high resolution. This diagnostic is able to measure the areal density in the region from 50 to 250 mg/cm^2—typical values achieved in recent experiments.

5.2.3 Neutron Temporal Diagnostic

The neutron temporal diagnostic (NTD) determines the fusion reaction-rate history by measuring the emission time of neutrons from DT- and D_2-filled targets. This instrument was previously operated on the Nova laser at LLNL[34] before being moved and adapted to the Omega facility. The instrument is based on a fast-rise-time, commercially available plastic scintillator and has a temporal resolution of 25 ps. Neutron collisions with the scintillator convert their kinetic energy to light with a wavelength between 350 and 450 nm. The light is collected and transported by an *f*/2 zoom-lens optical system to the photocathode of a fast streak camera, whose output image is recorded by a CCD camera. The recorded target burn history is synchronized to the incident laser pulse through simultaneously recorded timing fiducial pulses. The absolute-time calibration has been determined to an accuracy of 50 ps. The NTD needs neutron yields greater than 10^9 to obtain a usable burn history because of neutron statistics. Compared with the neutron bang-time detector (Sec. 5.2.4), the NTD has better temporal resolution but lower sensitivity because a streak camera is used instead of a photomultiplier tube.

The new, cryoNTD[10] has been developed to measure the fusion reaction history of D_2 cryogenic targets. The NTD must be withdrawn to a distance of 20 cm during cryogenic shots to avoid interference with the cryogenic equipment. As a result the NTD has insufficient sensitivity for D_2 cryogenic implosions, motivating the development of the cryoNTD. The cryoNTD is placed

in a ten-inch-manipulator port and uses a ~30-mm-diam scintillator placed at 9 cm from target chamber center. The cryoNTD uses the same fast scintillator as the NTD along with a similar streak camera and fiducial and similar analysis software. The cryoNTD sensitivity and temporal resolution are comparable to those of the NTD. The cryoNTD cannot be used for high-yield DT cryogenic implosions because its streak camera is not shielded against neutrons. However, for cryogenic DT targets, the sensitivity of the NTD at 20 cm from target chamber center is sufficient to measure the temporal burn history.

5.2.4 Neutron Bang-Time Detectors

The time interval from the beginning of the laser pulse to the peak of the neutron emission (the bang time) is an important parameter in inertial confinement fusion experiments. The neutron bang time is very sensitive to the energy absorption and the hydrodynamic response of the target and can be directly compared with numerical simulations.

The neutron bang-time detector (NBT) on OMEGA[41] uses fast quenched scintillators and fast photomultiplier tubes and can be used for yields up to 10^{11}. A new detector—the high-yield neutron bang-time detector (HYNBT)—has been developed to measure the bang time in high-yield experiments. The HYNBT is also a continuation of prototype diagnostic development work[45] for the National Ignition Facility.

A schematic of the HYNBT detector is shown in Fig. 5.7. It consists of three chemical-vapor-deposition (CVD) diamond detectors of different sizes and sensitivity placed in a lead-shielded housing. The HYNBT uses "optical quality" polycrystalline DIAFILM CVD wafers purchased commercially.[48] The CVD wafers are disks with the following dimensions: Ch1 10-mm diam, 0.5-mm thick; Ch2 5-mm diam, 0.25 mm thick; and Ch3 2-mm diam, 0.5-mm thick. The electrical contacts, consisting of 10-nm-thick Cr and 50-nm-thick Au, were deposited on each side of the CVD wafer. Each wafer was assembled in a separate, simple aluminum housing with an SMA connector. The separate housing for each channel allows pre-testing of the individual CVD diamond detectors. The HYNBT thin-wall stainless steel cylinder acts as a Faraday cage, decreasing electromagnetic pulse (EMP) noise. The HYNBT lead shielding protects the CVD diamond detectors from hard

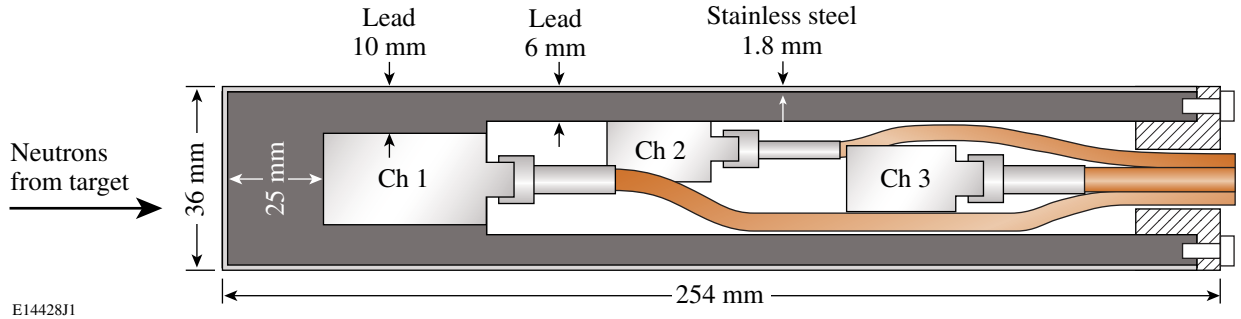

Figure 5.7
Design of the high-yield neutron bang-time (HYNBT) detector.

x rays. This shielding is not necessary for current experiments on OMEGA but it has been installed in anticipation of a higher level of hard x rays produced by the interaction of the short OMEGA EP laser pulse with the gold cone or the fuel shell in fast-ignition experiments.[49] Double-braided RG-142 coaxial cables are used to deliver the signals to an oscilloscope due to their low sensitivity to neutron-induced signals.[50] The HYNBT is used alternatively in the same re-entrant tube as the NBT at 50 cm from the target chamber center. The RG-142 cables are 10 m long and are followed by 22-m-long LMR-400 cables. Inside the OMEGA Target Bay the cables are routed in the radial direction as much as possible to minimize the interaction of neutrons with the cables. The LMR-400 cables have a higher bandwidth than RG-142 cables but much higher sensitivity to neutron-induced signals.[50] This two-cable solution is a compromise between high bandwidth and neutron-induced signal sensitivity. All HYNBT channels are biased at –750 V using a bias-T (Picosecond Pulse Labs, model 5531). The signals from the HYNBT CVD diamond detectors are recorded by three channels of a 3-GHz, 10-GS/s, Tektronix TDS-694 oscilloscope.[46] The OMEGA optical fiducial pulse train is recorded on the fourth oscilloscope channel using a fast photodiode to provide a time reference with respect to the laser pulse. The fiducial analysis and fitting procedure are described in Ref. 41.

The HYNBT has been tested on OMEGA for both DT and D_2 implosions. Figure 5.8 shows a typical oscilloscope trace for a shot yielding 4.4×10^{12} DT neutrons. Since the HYNBT is biased by a negative high voltage, the signals from CVD diamonds are positive and then inverted during analysis. The measured signals were fit by a convolution of a Gaussian and an exponential decay, as described in detail in Ref. 41. The time constant of the exponential decay (0.5 ns in Fig. 5.8) represents the carriers' collection time in the CVD diamond wafer. At a constant bias voltage, the time constant depends on the thickness and diameter of the CVD wafer. It must be determined once and can then be used for the analysis of all subsequent data. All other fit parameters are determined for every shot to account for trigger shifts and changes in bang time and ion temperature. The time of the pulse is defined to be the center of the Gaussian part of the fit. Figure 5.9 shows the signal amplitudes of all three HYNBT channels as a function of the DT neutron yield. The straight lines are linear fits to the data for each channel. The signal from the first HYNBT channel saturates above 100 V and the second channel saturates above 80 V. At a yield of 1×10^{15} the third channel will have a signal of ~20 V and will not be saturated. The three HYNBT channels can, therefore, measure the neutron

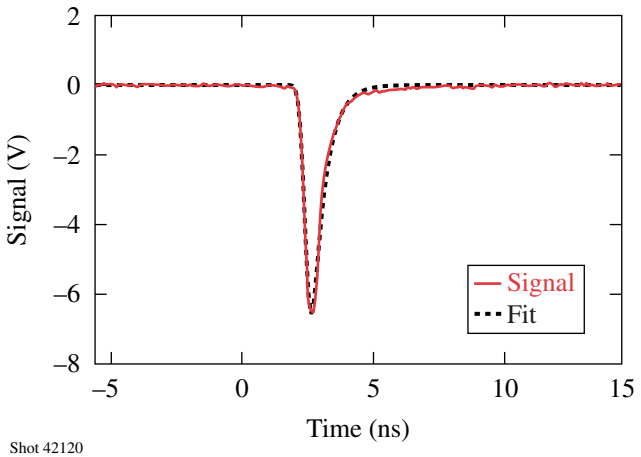

Figure 5.8
Channel-2 HYNBT signal for shot 42120 with a DT neutron yield of 4.4×10^{12}.

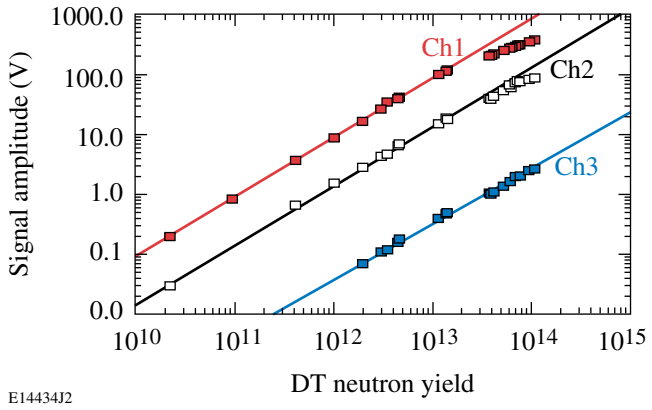

Figure 5.9
Signal amplitude of the HYNBT channels as a function of DT neutron yield.

bang time in DT implosions over the yield range from 1×10^{10} to 1×10^{15}. For D_2 implosions, the bang time can be measured for neutron yields above 3×10^{10}.

The timing accuracy of the HYNBT was studied by measuring the time difference among channels. The time difference between two channels recorded during two shot days with DT yields varying from 8.4×10^{12} to 3.5×10^{13} had an rms of 13 ps (Ref. 42). The HYNBT was tested five times during 2005 and in all cases demonstrated internal time resolution better than 20 ps. The timing calibration of the HYNBT bang time relative to the OMEGA laser pulse was established by cross calibration against the neutron temporal diagnostics (NTD). A good correlation between the two detectors was observed with an rms difference of 40 ps.

Only the first HYNBT channel is sensitive enough for D_2 implosions on OMEGA. The first channel has been cross calibrated against the NTD. EMP mitigation measures applied during the HYNBT design have reduced the EMP noise level about ten times relative to the NBT.[41] For all shots on OMEGA the EMP noise level in the HYNBT is below 4 mV.

More details about this work are found in Ref. 42.

5.2.5 Magnetic Recoil Spectrometer

The OMEGA magnetic recoil spectrometer (MRS)[51–56] was designed as a prototype of the NIF MRS to measure the absolute neutron spectrum in the range 5 to 30 MeV for the simultaneous determination of the areal density ρR, the neutron yield Y_n, the ion temperature T_i, and possibly nonthermal features in the neutron spectra. This instrument was designed specifically for use on OMEGA and has been operational since 2010. The principle of the MRS, wherein neutrons emerging from the implosion collide with a CH or CD target producing protons or deuterons that are energy analyzed, is shown schematically in Fig. 5.10 and the assembly as mounted on OMEGA is shown in Fig. 5.11.

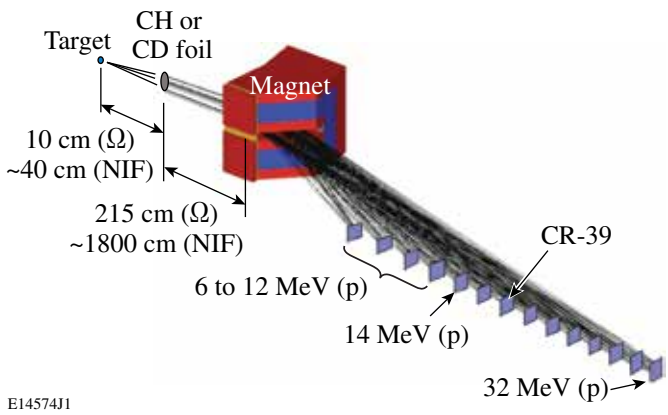

Figure 5.10
(a) Principle of the magnetic recoil spectrometer (MRS), which will be used to determine the areal density (ρR), the ion temperature (T_i), and the absolute neutron yield with high accuracy, first at OMEGA and then at the NIF. Forward-scattered protons from a CH foil (or deuterons from a CD foil) are momentum analyzed and focused by the magnet onto the detector.

Figure 5.11
Photograph of the magnetic recoil spectrometer (MRS) fully installed on OMEGA. The entire magnet and detector structure is contained within a polyethylene shield.

The OMEGA MRS immediately played an important role in OMEGA experiments. For ten years, the areal densities of imploded ICF targets on OMEGA have been measured by charged-particle spectrometers and wedge-range-filter proton spectrometers.

Representative deuteron spectra from the OMEGA MRS are shown in Fig. 5.12(a) for three low-adiabat, cryogenic DT implosions producing neutron yields in the range of 2×10^{12} to 4×10^{12}. The main differences in the deuteron spectra are seen in the 7- and 8-MeV channels and reflect large differences in the ρR values of the three implosions. The neutron spectra that best reproduce the observed deuteron spectra after convolution with the MRS response function (which includes slowing down of protons or deuterons within the foil) are shown in Fig. 5.12(b).

To infer the target ρR from these neutron spectra, use is made of the linear relationship between ρR and the ratio of the (measured) yield of down-scattered neutrons Y_{ds} to the total (measured) neutron yield Y_n:

$$\rho R \approx \frac{(2\gamma + 3)}{(\gamma\sigma_d + \sigma_t)} \frac{Y_{ds}}{Y_n}, \tag{5.2.1}$$

where γ is the ratio of the deuteron and triton number densities, σ_d and σ_t are the total neutron elastic-scattering cross sections with deuterons and tritons, respectively, and m_p is the proton mass.[56] The down-scattered yield Y_{ds} and the cross sections σ_d and σ_t may be defined for different neutron energy ranges; in Fig. 5.12(b), the areal densities were inferred from the down-scattered neutron yields in the 10- to 12-MeV range.

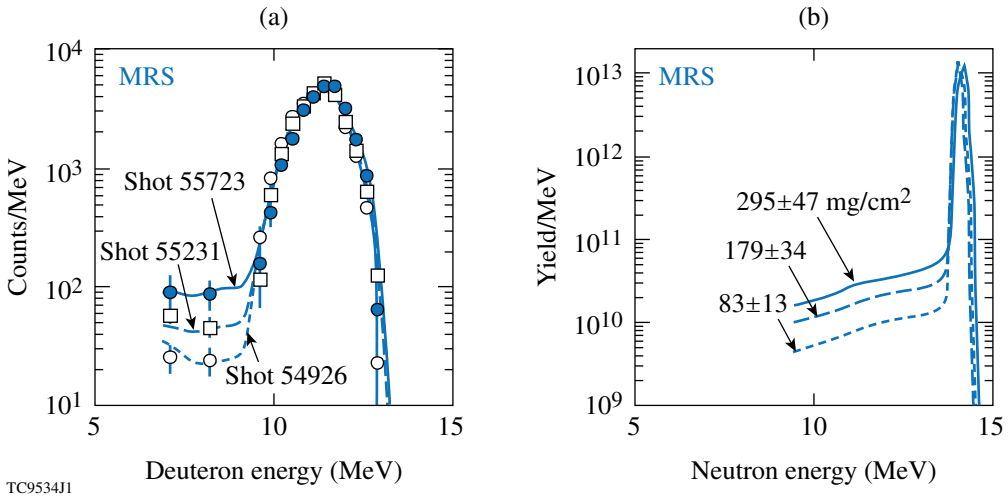

Figure 5.12
(a) MRS data (symbols) obtained using a CD foil for three low-adiabat, cryogenic DT implosions. Multiple data points are routinely obtained from different portions of a single CR-39 detector. (b) Modeled neutron spectra for the three shots, chosen so that when convolved with the MRS response function they result in the deuteron spectra (curves) in (a), fitting the data points. The inferred areal densities for the three shots are indicated in (b), based on the ratio of down-scattered neutrons to primary neutron.

In the first shot (54926), a cryogenic target was imploded with an $\alpha = 3$ laser pulse [α being the target adiabat] with incorrectly timed pickets in front of the main drive pulse leading to mistimed shocks. The inferred ρR was only 83±13 mg/cm^2. In the second shot (55231) a similar laser pulse was used but with the pickets correctly timed, and a larger ρR of 179±34 mg/cm^2 was inferred, closer to the 1-D *LILAC* prediction of 220 mg/cm^2. In the third shot (55723), an $\alpha = 2$ laser pulse with correct shock timing was used and a ρR of 295±47 mg/cm^2 was inferred, ~95% of the 1-D prediction for this pulse.

The OMEGA MRS has been cross calibrated against the well-established charged-particle spectrometers for low-ρR plastic capsule implosions. Charged particle spectrometer measurements of the knock-on deuteron spectrum have enabled the ρR of cryogenic DT implosions to be determined up to ~180 mg/cm^2 (Ref. 57); however, measurements of higher values of ρR must rely on the MRS data.

5.3 X-RAY IMAGING

Imaging of laser-generated plasma x-ray emission is used to determine the size, shape, temperature, and areal density of compressed plasmas at LLE. Time-integrated x-ray emission is imaged with pinhole cameras (Sec. 5.3.1) and Kirkpatrick–Baez (KB) microscopes (Sec. 5.3.3). One KB x-ray optic is incorporated into the gated monochromatic x-ray imager (Sec. 5.3.4), which is capable of recording time-resolved x-ray images using custom framing cameras. Images from these diagnostics are recorded using film, image plates, and solid-state cameras. Another set of x-ray framing cameras record time-resolved x-ray images using either film or CCD cameras.

Temporal data are obtained from x-ray streak cameras (Sec. 5.4) and a time-resolved hard x-ray detector (Sec. 5.5.1). Hard x rays may be imaged with an x-ray image-plate diagnostic.

5.3.1 X-Ray Pinhole Cameras

X-ray pinhole cameras (XRPHC's) are a much used diagnostic on both the OMEGA and OMEGA EP target chambers. They are currently available with digital readout using direct x-ray–detecting, charge-injection–device (CID)[58] cameras. These cameras allow for quick processing of x-ray images obtained on target experiments. X-ray emission is typically detected from a target for all regions where the laser intensity exceeds 10^{14} W/cm^2. XRPHC images are used for precision pointing of the OMEGA laser beams,[59] beam-focus determination, target-position determination, verification of main-target and backlighter-target positions, and alignment of the OMEGA EP beam relative to the OMEGA target chamber center. The imaging is accomplished with a single 10-μm-diam pinhole laser drilled into a Ta foil. The typical target-to-pinhole distance is 17 cm, while the pinhole-to-CID-camera distance is typically 68 cm for a magnification of 4. The unobstructed field of view of the camera in this case is ~6 mm at the target plane. This allows one to use the cameras to observe both standard-size imploding targets (~0.9-mm diam) and larger-size targets such as x-ray pointing targets (4-mm diam). Both fixed pinhole cameras and TIM-based pinhole cameras are available, and as many as 11 are used simultaneously (5 fixed and 6 TIM-based, Table 5.2) when precision beam pointing (accuracy better than 10 μm) is required. Three fixed XRPHC's and five TIM-based XRPHC's are available on the OMEGA EP target chamber (Table 5.3). The OMEGA XRPHC's use 50.8-μm-thick Ta pinhole substrates, while the OMEGA EP cameras use 254-μm-thick Ta substrates. This suppresses the throughput of very hard x rays (>100 keV) generated by the OMEGA EP beams when they are operated in high-intensity mode (>10^{18} W/cm^2), allowing for better detection of the soft x rays emitted by the target.

5.3.1.1 CID camera readout system

OMEGA and OMEGA EP use charge-injection devices[58] (CID's) to electronically record the time-integrated, spatially dependent x-ray flux distribution in imaging instruments. The CID-camera readout systems provide up to 18 camera readouts on OMEGA and up to 12 camera readouts on OMEGA EP. The current cameras use 800 × 600-pixel arrays with 38.5 × 38.5-μm-sq pixels. The readout systems are interfaced to all the fixed x-ray pinhole cameras, all the TIM-based, time-integrated x-ray diagnostics [including x-ray spectrometers and NLUF (National Laser Users' Facility) user–supplied instruments], and the KB microscopes (including the GMXI). Because of

their electronic architecture,[60] these cameras are durable detectors suited to the extreme radiation conditions that can be generated in the OMEGA target chamber. Located as close to the target as 0.8 m, they provide useful images even on shots producing the highest neutron yields (up to ~10^{14} for DT) that can be generated on OMEGA.[61]

The target position relative to the laser beam aiming at the time of an experiment determines the symmetry of the laser illumination of the target. The XRPHC's outfitted with CID cameras have proven to be invaluable in determining the precise target position post-shot since they routinely acquire images from which the target position at the beginning of the laser pulse can be determined. This is particularly important for cryogenic target experiments,[62] where the addition of the moving cryostat increases the difficulty of positioning the target relative to the point to which the laser beams are aimed.

Table 5.2: Specifications of OMEGA x-ray pinhole cameras.

Port	(θ, ϕ)	Type	Magnification	Pinhole Diameter	Pinhole Thickness
H4F	(45.23, 234.00)	Fixed	4.0	10 μm	50.8 μm
H8C	(79.30, 153.78)	Fixed	2.06	10 μm	50.8 μm
H12C	(108.89, 54.00)	Fixed	4.0	10 μm	50.8 μm
H13C	(92.74, 342.00)	Fixed	4.0	10 μm	50.8 μm
P11D	(113.90, 238.89)	Fixed	4.0	10 μm	50.8 μm
TIM 1/P3	(63.44, 126.00)	TIM-based	1 to 4	10 μm	50.8 μm
TIM 2/H3	(37.38, 162.00)	TIM-based	1 to 4	10 μm	50.8 μm
TIM 3/H18	(142.62, 342.00)	TIM-based	1 to 4	10 μm	50.8 μm
TIM 4/P6	(63.44, 342.00)	TIM-based	1 to 4	10 μm	50.8 μm
TIM 5/H7	(79.19, 90.00)	TIM-based	1 to 4	10 μm	50.8 μm
TIM 6/P7	(116.57, 162.00)	TIM-based	1 to 4	10 μm	50.8 μm

Table 5.3: Specifications of OMEGA EP x-ray pinhole cameras.

Port	(θ, ϕ)	Type	Magnification	Pinhole Diameter	Pinhole Thickness
P39	(74, 253)	Fixed	4.0	10 μm	254 μm
P47A	(66, 95.14)	Fixed	4.0	10 μm	254 μm
P52A	(66, 90)	Fixed	1.7	10 μm	254 μm
TIM 10/P2	(27, 0)	TIM-based	1 to 4	10 μm	254 μm
TIM 11/P9A	(39, 189)	TIM-based	1 to 4	10 μm	254 μm
TIM 12/P45	(90, 0)	TIM-based	1 to 4	10 μm	254 μm
TIM 13/P87	(153, 180)	TIM-based	1 to 4	10 μm	254 μm
TIM 14/P48	(90, 90)	TIM-based	1 to 4	10 μm	254 μm

5.3.2 X-Ray Framing Cameras

X-ray framing cameras[63–69] are used for two-dimensional, time-resolved imaging. Three framing cameras are available, of which one is operated with a temporal resolution of ~40 ps, and three are operated with 200, 300, 400, 500, or 1000-ps resolution by the use of interchangeable pulse-forming modules. The framing cameras are operated from ten-inch manipulators (TIM's, Sec. 4.4.2). An additional 40-ps framing camera has been transferred to the NIF.

The key component of a framing camera is a microchannel plate (MCP), which has a gold photocathode coated onto its surface in the form of a microstrip line. A two-dimensional x-ray image is formed on the photocathode, producing photoelectrons that are accelerated down the channels of the MCP and multiplied by a short-duration, high-voltage pulse. As this pulse propagates along the microstrip line, different sections of the microstrip line are sequentially gated. The electrons exiting the MCP strike a phosphor plate, producing an optical image.

The optical image is recorded with either film or a CCD (charge-coupled device) camera with 4096×4096 pixels of 9-μm size. Currently, all of the six TIM's on the OMEGA target chamber are outfitted to accept CCD recording systems, and up to three CCD cameras can be used simultaneously. In the future, all TIM's on OMEGA and OMEGA EP will be capable of using CCD's. The CCD cameras are cooled to about –20°C during shot operations to reduce the CCD dark-current noise. All the framing cameras are now configured with remote electronic controls by which changes can be made to the camera's timing and MCP bias voltages through a computer interface, eliminating the need to cycle the framing camera to atmosphere every time these changes are required.

The fast (40-ps) framing camera is configured with a four-strip MCP, but the slow framing cameras can be configured to operate with a four-strip, two-strip, or single-strip MCP, depending on the needs of the particular experiment.

5.3.3 Kirkpatrick–Baez Microscopes

The Kirkpatrick–Baez (KB) microscopes used on OMEGA and OMEGA EP are derived from an original LLE design.[70] The reflection optics consist of four mutually perpendicular, stacked concave mirrors with a radius of curvature of ~26 m. The available KB optics for OMEGA and OMEGA EP are listed in Table 5.4 and are more fully described elsewhere.[71–75] Three are currently in use on the OMEGA and OMEGA EP target chambers. Two others are designed to couple to the PJX streak camera (Sec. 5.4). The resolution of the KB optic is limited by aberrations, primarily spherical, which depend on the mirror size. The smaller mirrors (optics #3 and #4) have better on-axis (~3 μm) and off-axis resolution but subtend smaller solid angles.

The energy range of the optic is determined by the coating on the reflecting surfaces. For optimum broadband imaging, three of the KB optics are coated with Ir, which has the best high-energy response of any elemental amorphous coating. Optics #1, #2, and #3 are Ir coated and provide broadband throughput from 2 to 8 keV. Optic #1, formerly in KB microscope KB1, was removed to accommodate passage of the OMEGA EP beams into the OMEGA target chamber. Optic #2 is

Table 5.4: LLE Kirkpatrick–Baez microscope specifications.

Optic #	Location	Coating	Magnification	Solid Angle (ster)	Energy Range (keV)
1	---	Ir	12.9	4×10^{-7}	2 to 8
2	OMEGA H12/GMXI	Ir	13.6	4×10^{-7}	2 to 8
3	OMEGA H13/KB3	Ir	12.9	1×10^{-7}	2 to 7
4	---	none	13.6	1×10^{-7}	1.5 to 3
5	OMEGA EP P74/ EPKBMIC	WB_4C	13.6	4×10^{-7}	7 to 9

identical to optic #1 and is installed in the gated monochromatic x-ray imager (GMXI), which records monochromatic images of target emission (Sec. 5.3.4). Optic #3, currently used in H13/KB3, has a grating installed to obtain space-resolved continuum spectra of target core emission.[71] Another optic (#4) is uncoated (bare Zerodur[74]) to provide for an energy throughput with no appreciable response above 3 keV. This optic is suited for the radiography of targets such as driven CH foils.[75] Optic #5 (Ref. 75) has a high-energy response defined by the multilayer coating applied to the reflecting surfaces (WB_4C, with the Bragg plane spacing $2d$ = 140 Å) and the standard grazing angle (0.7°). This optic is particularly useful for imaging high-opacity targets that emit x rays in the energy range 7 to 9 keV and is currently installed in the OMEGA EP EPKBMIC diagnostic, which uses a fixed microscope design identical to that used on OMEGA.

Work on a 16-image version of a KB microscope[76] is currently underway. A framing camera is also under development that will make it possible for gated images of target x-ray emission to be obtained using the 16-image KB optic as the imaging device.[76] The framing camera images will be obtained outside the vacuum system, allowing the instrument to be used on high-yield DT target experiments. This instrument is being developed with the goal of obtaining either self-emission or backlit images of cryogenic DT target implosions on OMEGA.

5.3.4 Gated Monochromatic X-Ray Imager (GMXI)

The GMXI is an instrument capable of simultaneously resolving x-ray emission from ICF targets in space, time, and spectrum.[73] Jointly developed by LLE and LANL, the GMXI consists of a KB microscope and two monochromator/imager pairs. WB_4C multilayers (with $2d$ = 26.5 Å) coated onto smooth Si(111) substrates allow one to image narrow energy bands ($\Delta E \sim 10$ eV) with no additional blurring from the monochromator. The imagers can be film packs, CID cameras, or custom framing cameras.[73] When used in the time-integrated mode, both film packs and CID cameras can be used simultaneously, or up to four CID cameras can be used. Each monochromator turret holds two monochromators at the same angle and can be tuned to a different energy. The optic used in the GMXI (optic #2 of Table 5.4) has a useful energy range from 2 to 8 keV.

5.3.5 X-Ray Backlighter Capabilities

X-ray radiography continues to be a valuable diagnostic tool for characterizing high-energy-density plasmas. Many experiments, including studies of laser imprinting, the growth of perturbations

due to the Rayleigh–Taylor instability, and jet propagation in low-density media, have used large area x-ray backlighters. In this geometry the object is placed between the x-ray source and an x-ray imager, and the area of the backlighter spot is typically a little bigger than the area of the object. Primary x-ray imagers are variants of pinhole cameras with the pinhole providing spatial resolution of the x-ray absorption. X-ray microscopes (Sec. 5.3.3) are also used, with the spatial resolution being provided by the x-ray optics.

The signal-to-noise ratio, uniformity, and field of view of these radiographs are limited by the size and uniformity of the emission from the large-area backlighters. An alternate radiographic technique—point-projection backlighting[77,78]—has, therefore, been developed for use on the OMEGA laser. This uses the backlighter itself as the imaging device. The concept of point-projection backlighting is not new, but its development and use on OMEGA have increased substantially over the past few years.

A schematic of a point-projection backlighter is shown in Fig. 5.13. A point source of x rays casts a shadow of the plasma being characterized onto a large-format x-ray detector. Encoded into the shadow data is the transmission through the plasma along the path from the x-ray source to the detector. The signal-to-noise ratio, uniformity, and field of view of the measurement are no longer limited by the uniformity of a large-area backlighter; they are limited only by the uniformity of x-ray emission into the solid angle subtended by the detector and self-emission from the object being radiographed. The spatial resolution is defined by the spatial size of the x-ray emitter just as the size of a pinhole defines the spatial resolution of a pinhole camera.

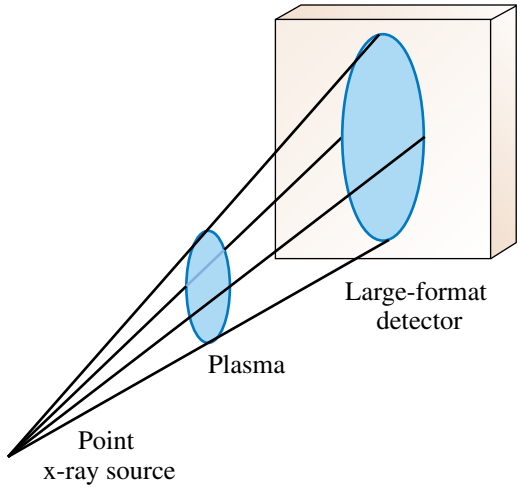

Figure 5.13
Schematic of a point-projection backlighter. The point x-ray source casts an image onto the detector from x rays that pass through the plasma being radiographed. The image is magnified by the ratio of the distance of the detector from the source to the distance of the plasma from the source.

Two point-projection backlighter configurations are shown in Fig. 5.14. Both configurations use a foil as an x-ray emitter and a substrate with a pinhole to limit the spatial extent of the x rays reaching the detector. Figure 5.14(a) shows the simplest scheme, where the x-ray emission foil is mounted directly onto the pinhole substrate with the laser beams needed to create the x rays incident on the rear surface. This geometry requires that the x-ray emission foil be transparent to the x rays used for radiography. In Fig. 5.14(b), the x-ray emission foil is mounted to the pinhole substrate at

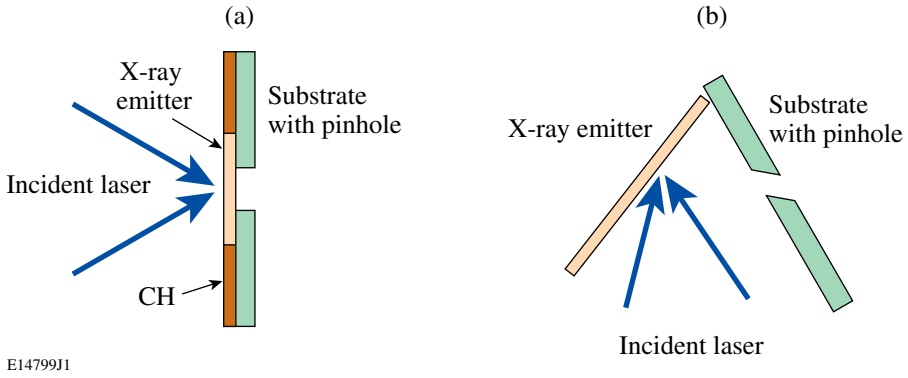

Figure 5.14
Two point-projection backlighter configurations. In (a) the laser beams are incident onto the rear surface of a target composed of an x-ray emitter bonded to a substrate with a pinhole. In (b) the laser is incident onto the front surface of the x-ray emitter with the substrate at an angle to the x-ray emitter. The pinhole in (b) is drilled at an angle relative to the substrate surface.

a large enough angle so that the laser beams can illuminate the front surface of the x-ray emitter. The pinhole in the substrate must then be at an angle relative to the substrate surface. Both of these configurations have been used on OMEGA experiments and have proven to be valuable tools for diagnosing high-energy-density plasmas.

The rear-surface point-projection backlighter is limited to x-ray emitters for which the Lyman-α and/or helium-α lines from the laser illumination of the emission foil have lower energies than the nearest absorption edge. For K-shell emitters, this is true only for elements with Z greater than or equal to that of chlorine. This may be seen from Table 5.5, which lists common x-ray emitters for backlighting together with their K absorption edge and Lyman-α and helium-α

Table 5.5: Common K-shell x-ray emitters with their K-edge, Lyman-α, and helium-α x-ray energies (in keV).

Element	K edge	Ly α	He α
Mg	1.303	1.4717	1.3432
Al	1.55898	1.7277	1.5883
Si	1.839	2.0043	1.8539
Cl	2.833	2.9585	2.7751
Sc	4.492	4.523	4.295
Ti	4.966	4.966	4.727
V	5.465	5.431	5.18
Fe	7.112	6.952	6.668
Ni	8.333	8.073	7.766
Cu	8.979	8.593	8.28
Zn	9.659	9.281	8.95

emission energies. Chlorine is the lowest-atomic-number element whose helium-α emission has a lower energy than the K-absorption edge. A thin emitter foil will, therefore, be transparent to these x rays. The lowest-atomic-number element that is transparent to both the Lyman-α and the helium-α emissions is vanadium.

A point-projection backlighter with the geometry shown in Fig. 5.15(a) has been characterized with three different detectors: a single-strip x-ray framing camera, Kodak Biomax MS film, and an x-ray-sensitive CCD array. The backlighter assembly consisted of a 25-μm-diam pinhole in the center of a 5-mm × 5-mm, 50-μm-thick Ta foil with 100 μm of CH on both foil faces. The x rays were emitted by a 200-μm-diam, 5-μm-thick V foil illuminated by 2 to 21 beams from the OMEGA laser in the direction toward the detector. The detector has a large open aperture protected by a 5-μm-thick V foil, so any debris created by the pinhole assembly has the potential to damage the detector. The backlighter assembly shown in Fig. 5.14(a) has been shown to minimize shrapnel-like debris that could cause damage. Edge response data for all three detectors for a two-beam shot with a 1-ns, temporally flat pulse are shown in Fig. 5.15. The data are fit very well with an error function, consistent with a Gaussian point-spread function. There is little difference in the measured resolution for the three detectors. The equivalent full width at half maximum of the point-spread function for the framing camera, film, and CCD array are 13±1 μm, 13±1 μm, and 15±1 μm, respectively.

Point-projection backlighting can also be applied to the phase-contrast imaging of high-energy-density plasmas. Small point sources are critical for this application.

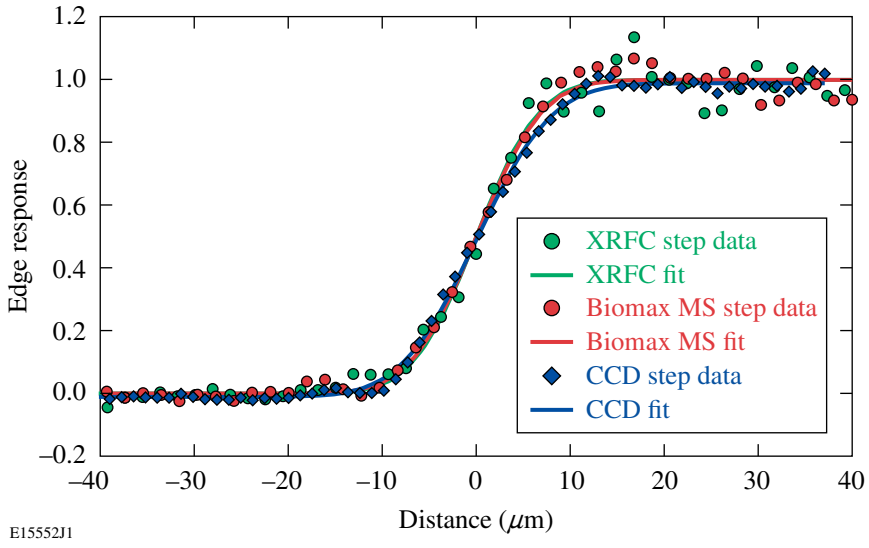

Figure 5.15
Spatial resolution of a V point-projection backlighter measured by recording an edge response for an x-ray framing camera (XRFC, green points), Kodak Biomax MS film (red points), and an x-ray-sensitive CCD array (blue points). The measured data were fit with error functions, assuming a Gaussian point-spread function.

5.3.6 Short-Pulse Backlighter Development

Ultrashort (<20 ps), bright x-ray backlighter sources in the 2-keV photon energy range will be provided by OMEGA EP to image cryogenic spherical implosions close to stagnation. Simulations have shown that ~2-keV x rays are optimum for the high-contrast radiography of imploded cores at the time of peak neutron production (typically with temperature ~1 keV and areal density ρR ~200 mg/cm^2). A framing-camera gating time of ~20 ps is envisaged in order to minimize motional blurring and the contribution from target self-emission.

Preliminary experiments were performed on the Vulcan laser at the Rutherford Appleton Laboratory, UK, to measure aluminum K-shell x-ray emission in the 1.6- to 2.0-keV range. The ultrashort-pulse Vulcan 100 TW[79] and Petawatt[80] laser facilities were used to irradiate small aluminum foil targets. The *p*-polarized laser beams were focused at a 30° angle of incidence with *f*/3 off-axis parabolas to a spot size of ~10 μm in diameter on thin foils with an area of 100 × 100 μm^2. The targets at the 100-TW facility were mounted as 20-μm-thick flags on carbon fibers of 6-μm diameter [Fig. 5.16(a)], while the targets at the Petawatt facility were suspended by two thin spider-silk fibers [Fig. 5.16(b)] to reduce the coupling of electron current into the target mount and to minimize thermal losses. The full short-pulse capability of the 100-TW facility (0.5 ps) was not used for these experiments; instead, the Vulcan laser produced a 14-ps pulse and a pulse energy of ~100 J, to result in a maximum on-target intensity of 1 × 10^{18} W/cm^2. For the experiments at the Petawatt facility, the laser had a 0.4-ps pulse duration and a pulse energy of ~530 J, resulting in 4 × 10^{20} W/cm^2 on target at the tightest focus.

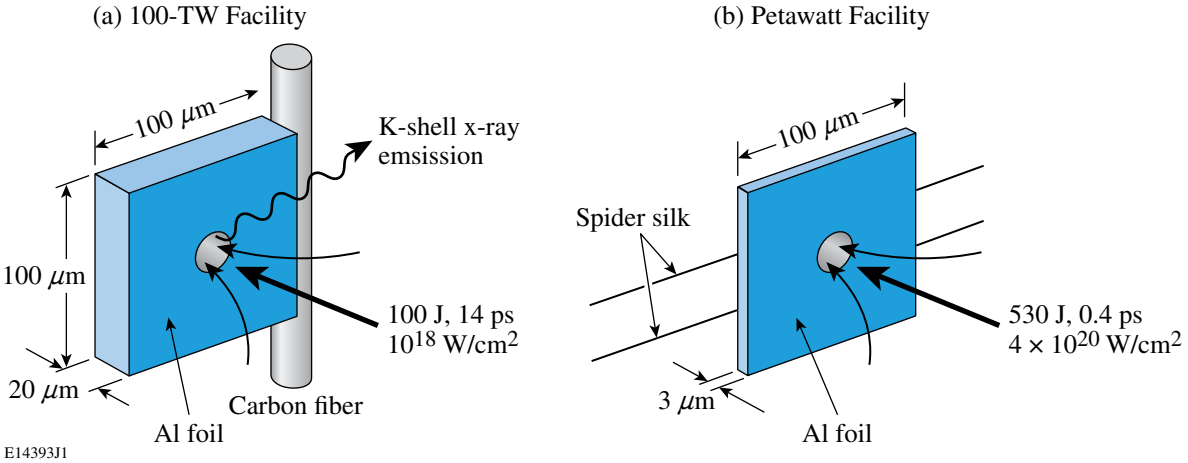

Figure 5.16
Aluminum foil targets with an area of 100 × 100 μm^2, (a) mounted as flags on carbon fibers for experiments on the 100-TW facility and (b) suspended by thin spider-silk fibers for experiments on the Petawatt facility of the Rutherford Appleton Laboratory Vulcan laser system. Ultrashort pulses were focused onto the foils and the Al K-shell emission was measured.

X-ray spectrometers equipped with potassium acid phthalate (KAP) crystals ($2d = 26.63$ Å) recorded the plasma emission from the laser-irradiated side at a viewing angle of 16° with respect to the target normal. Figure 5.17(a) shows the results for two laser intensities using the 100-TW facility. The lower intensity of 10^{16} W/cm^2 was obtained by defocusing the laser to a ~100-μm spot diameter while keeping the laser energy at ~100 J and the pulse duration at 14 ps. The emission consists of the He$_\alpha$ (1.59 keV) and Ly$_\alpha$ (1.73 keV) transitions of the helium- and hydrogen-like ions and several satellite lines on the lower-energy side of each resonance line. For the higher laser intensity of 10^{18} W/cm^2, the spectral energies of the He$_\alpha$ and Ly$_\alpha$ lines are larger by factors of 2.5 and 10, respectively, and a significant increase in the spectral line widths is observed.

The radiated spectral energy densities in units of mJ/eV were estimated by using the detector quantum efficiency, filter transmissions, the crystal diffraction efficiency, and the solid angle of the spectrograph. The quantum efficiency was obtained from K$_\alpha$ measurements in single-photon counting mode, making assumptions for the photon absorption probability in the CCD chip.[81] The absorption of an x-ray photon creates a certain number of free charge carriers proportional to the photon energy. K$_\alpha$ measurements of various target materials yielded the value of 4.56-eV absorbed energy per count per pixel for the CCD detector. The absorption probability for 1.6- to 2.0-keV photons in a typical 20-μm-thick silicon depletion layer is in the range 75%–100%. Since the exact depletion-layer thickness is not known, a 100% absorption probability was assumed. Peak spectral energy densities of ~7 mJ/eV (He$_\alpha$) and ~4 mJ/eV (Ly$_\alpha$) were inferred assuming isotropic emission into a 4π solid angle. The absolute uncertainty is estimated to be a factor of 3 based on the fact that no absolute calibration of the spectrometers was performed.

Calculations with the commercially available *PrismSPECT* program[82] were performed to estimate the plasma conditions in the laser-heated foil targets. The plasmas were assumed to be in steady-state, nonlocal-thermodynamic-equilibrium conditions in slab geometry and to have a

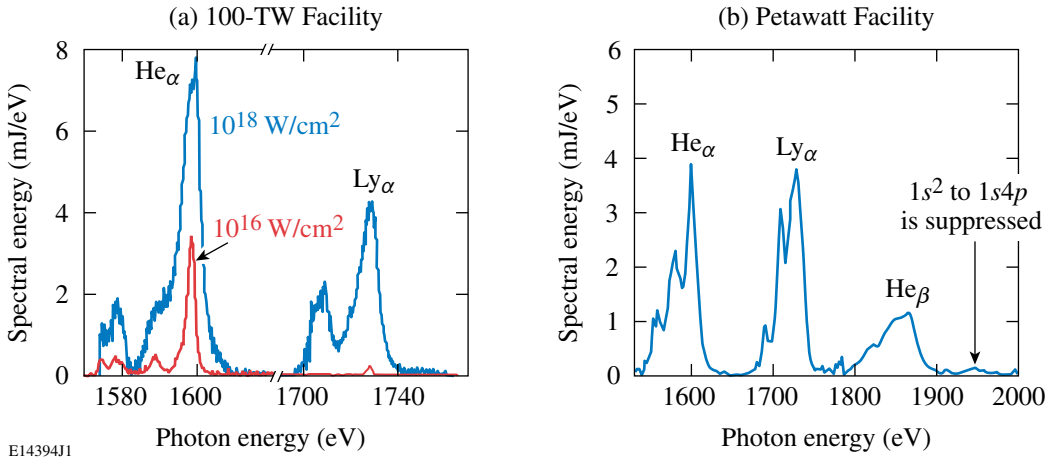

Figure 5.17
Aluminum K-shell emission from Vulcan experiments on (a) the 100-TW and (b) the Petawatt facilities. A larger spectral range was available in (b). Electron densities and temperatures of up to (a) $n_e = 8 \times 10^{22}$ cm^{-3} and $T_e = 400$ eV and (b) $n_e = 2$ to 4×10^{23} cm^{-3} and $T_e = 500$ to 600 eV are inferred.

homogeneous density and electron temperature over a specified thickness. The temporally and spatially averaged electron temperature and density were found to be T_e = 300 eV and $n_e = 3 \times 10^{21}$ cm^{-3} for the 1×10^{16} W/cm^2 measurement, while a strongly increased density of 8×10^{22} cm^{-3} and a slightly higher temperature of 400 eV were inferred for 1×10^{18} W/cm^2 (Ref. 83). A possible explanation for the difference in density might be pre-plasma formation by a laser-pulse pedestal, induced by amplified spontaneous emission, that causes some ablation of the front layer before the main laser pulse impinges on the target. The main pulse then interacts with plasma at less than solid density and an increased density scale length. At laser intensities below 1×10^{18} W/cm^2 the ponderomotive force is probably insufficient to push the underdense plasma out of the beam path and the laser energy is mainly deposited below the critical density, while for higher intensities "hole boring" creates a channel in the preformed plasma and the laser energy is deposited in a near-solid-density plasma.

The result for a 3-μm-thick, spider-silk–mounted target that was irradiated at the Petawatt facility at 4×10^{20} W/cm^2 is shown in Fig. 5.17(b). Higher densities and temperatures are inferred with $n_e \sim 2$ to 4×10^{23} cm^{-3}, which is close to solid density ($n_e = 7.8 \times 10^{23}$ cm^{-3}), and $T_e \sim 500$ to 600 eV. The overall spectral energy is slightly lower than for the 20-μm foil target, probably due to the smaller number of emitters in the thinner foil target. Rapid temporal changes in the density and temperature are expected in these highly transient short-pulse-laser–produced plasmas together with strong gradients in the longitudinal and radial directions. Isochoric heating of foil targets to a depth of ~15 μm with temperatures of up to 500 eV was recently reported[84] for solid-density foils and buried Al tracer layers irradiated at the Petawatt facility at intensities of ~10^{20} W/cm^2. In contrast, a hot surface layer with a 2- to 3-keV electron temperature and a depth of 1 μm was observed[85] in the interaction of a 0.7-ps Petawatt laser beam with solid copper-foil targets at 3×10^{20} W/cm^2. The densities and temperatures inferred from the Al K-shell emission are close to the values reported in Ref. 85, showing that the bulk emission from the isochorically heated solid material dominates.

The measured time-integrated spectral energy densities are encouraging for the development of a short-pulse backlighter source. Assuming an emission time of ~20 ps and a peak spectral energy density of 7 mJ/eV, this corresponds to a spectral power density of ~350 μJ/(eV·ps) into 4π steradians, which is a factor of ~3.5 higher than the predicted self-emission in the 2-keV range of an imploded cryogenic target at stagnation. Absolute time-integrated measurements of the cryogenic target self-emission are underway to provide a better estimate. Simulations have shown that backlighter spectral power densities of 800 μJ/(eV·ps) are required to obtain high-contrast radiographs at stagnation. Improved estimates of the spectral power density will require measurement of the temporal evolution of the backlighter source. Such experiments are proposed for OMEGA EP.

5.4 X-RAY STREAK CAMERAS

Existing x-ray streak cameras at LLE have demonstrated 10-ps time resolution, but this is insufficient for the experimental programs of OMEGA EP, where it is necessary to diagnose plasmas produced by 1- to 10-ps laser pulses. This has led to the development of an ultrafast x-ray streak camera (UFXRSC). The UFXRSC is TIM based, resides in an air bubble similar to the PJX streak camera, and utilizes the robust electronics that are employed on the successful ROSS (Rochester Optical Streak System[86]) platform.

The two main factors limiting the time resolution are (1) the chromatic dispersion of the secondary electrons in flight from the photocathode to the screen and (2) the streak speed that sets the time for the line image to cross its own width. The chromatic dispersion is caused by the initial energy spread of the secondary electrons emitted from the photocathode and is a basic property of the photocathode material[87] (the energy spread is 1.3 eV for KBr and <0.5 eV for 264-nm light on Au). This is mitigated by accelerating the electrons to the anode potential (12 kV) as quickly as possible. The streak speed is maximized by optimizing the ramp driver for a single speed (650-ps full screen) rather than the slower, remotely selectable four speeds available on the ROSS cameras. The P860 streak tube from Photonis[88] was selected for the UFXRSC. This is the open-geometry version of the P820 streak tube employed in all of LLE's optical VISAR diagnostics (Sec. 5.8) and the PDF-ROSS camera in OMEGA EP. The x-ray streak camera system was designed and built in collaboration with Sydor Instruments.[89]

It is well known that electrostatic deflection introduces electron-optical aberrations on the electron beam. The main effect is a parabolic image-plane curvature in the temporal direction of the streak image. The static streak-tube focus can be adjusted so that the paraxial region or some off-axis position is in best focus. However, for very fast streak speeds (where the electron beam traverses the anode at >5% of the speed of light) there is dynamic defocusing of the electron beam that causes the curved focal plane to shift away from the screen and become asymmetric and centered off-axis. Refocusing the tube to best compensate for this aberration is done experimentally. The MTW laser was used to produce 1-ps–duration UV (264-nm) pulses that were detected with a gold photocathode. A 6-mm-thick slab of fused silica was inserted over half the photocathode, producing a delayed pulse that was used to calibrate the time axis. The data presented in Fig. 5.18 show the camera-limited time resolution as a function of image-plane position when the camera is operated for optimum static focus in the paraxial region, and when it is refocused to shift the image plane ~10 mm along the tube axis and biased to center the region of best focus. A temporal resolution of <2 ps is demonstrated over three-quarters of the image plane. An electron-optical model of the streak tube can be used to calculate the time-resolution degradation when the initial electron energy spread is changed, corresponding to a change in the photocathode. The best time resolution with the KBr x-ray photocathode is predicted to be 2 ps.

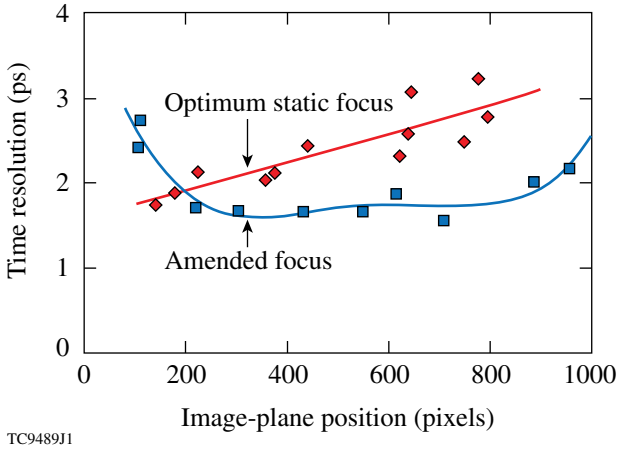

Figure 5.18
Camera-limited time resolution (FWHM) as a function of image-plane position obtained using 1-ps, 264-nm pulses on a gold photocathode. The diamonds correspond to operation with optimum static focus in the paraxial region, and the squares correspond to operation with the camera refocused to shift the image plane ~10 mm axially and biased to center the region of best focus. The lines are fits to the data.

The UFXRSC is in active use on OMEGA EP and the MTW. It has been used on hot-electron–generation experiments on OMEGA EP[90] and for experiments on the MTW to diagnose hot-electron lifetimes for laser intensities above 10^{18} W/cm^2 from time-resolved K_α measurements.[91] It has also been coupled to a Bragg crystal imager to diagnose the expansion of the K_α emission zone across the target surface.

5.5 HARD X-RAY DETECTOR

5.5.1 Time-Resolved Hard X-Ray Detector on OMEGA EP

The multichannel, time-resolved hard x-ray detector on OMEGA EP (EP-HXRD) is based on the successful OMEGA design.[92] Each of the four EP-HXRD channels is filtered by a single high-pass filter, very similar to the OMEGA HXRD with cutoff energies of 40, 40, 60, and 70 keV, respectively. The temperature T of the exponential tail of the hard x-ray spectrum can be inferred using the same methods as for the OMEGA HXRD. Figure 5.19 shows a CAD model of the four-channel detector mounted on port 70 of the OMEGA EP target chamber.

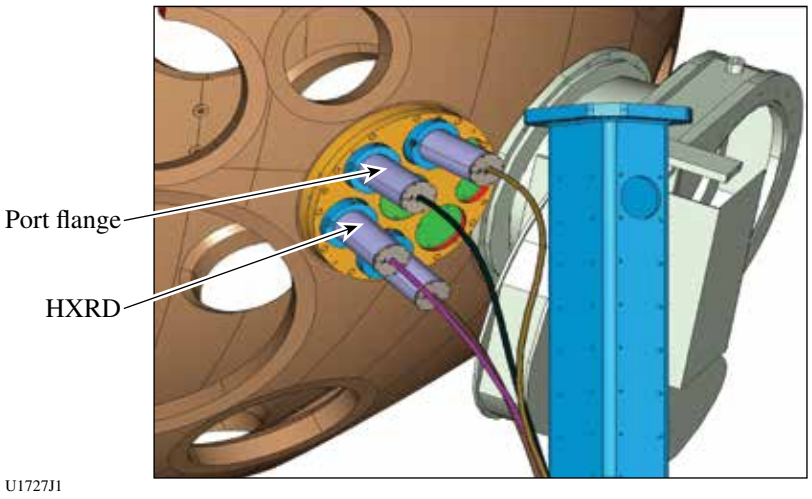

Figure 5.19
CAD model of the EP-HXRD installed on port 70 of the OMEGA EP target chamber. Four channels are mounted on four sub-ports of the large port flange.

5.6 TIM-BASED X-RAY CRYSTAL SPECTROMETERS

5.6.1 Spherical Crystal Imagers

Narrowband x-ray imagers using spherically bent crystals have been implemented on both laser facilities (OMEGA EP and OMEGA) at the University of Rochester's Laboratory for Laser Energetics. These spherical crystal imagers (SCI's) use a 150-μm-thick, 25.4-mm-diam quartz crystal cut either along the 2131 plane to reflect the Cu K_α line at ~8 keV with a Bragg angle of 88.7° or

along the 1011 plane to reflect the Si He_α line at ~1.865 keV with a Bragg angle of 83.9°. The SCI systems can be set up to either image the self-emission of a laser-heated target or to backlight a high-energy-density plasma object.

Imaging systems with spherically bent Bragg reflectors have unique capabilities that are advantageous when imaging laser–target interactions. A narrow spectral width [$\lambda/\Delta\lambda$ >1000] and a potentially high spatial resolution [<10 μm] can be achieved with high-quality crystals. The large solid angle subtended by the crystals provides a high throughput, which can be up to 100× larger than a conventional pinhole imager. Crystal imagers can be set up in either the (a) self-emission or (b) backlighter mode (see Fig. 5.20). When in backlighting mode, the backlighter target is placed out of focus. Therefore, any spatial nonuniformities in the laser-intensity distribution on the backlighter are washed out because of the limited depth of field. The high throughput, along with the narrow spectral width reflected from the crystal, is ideal for backlighting bright, high-energy-density plasma objects like a directly driven implosion target. LLE has been developing spherical crystal imaging (SCI) systems since early 2010. SCI systems have been installed on both laser facilities within LLE. The crystal imaging systems deployed at LLE are all based on 25.4-mm-diam, 150-μm-thick quartz crystals. These crystals are optically bonded to a 30.0-mm-diam spherical substrate with a 500-mm radius of curvature. The crystals are cut either along the 2131 planes for a 2d spacing of 0.3082 nm

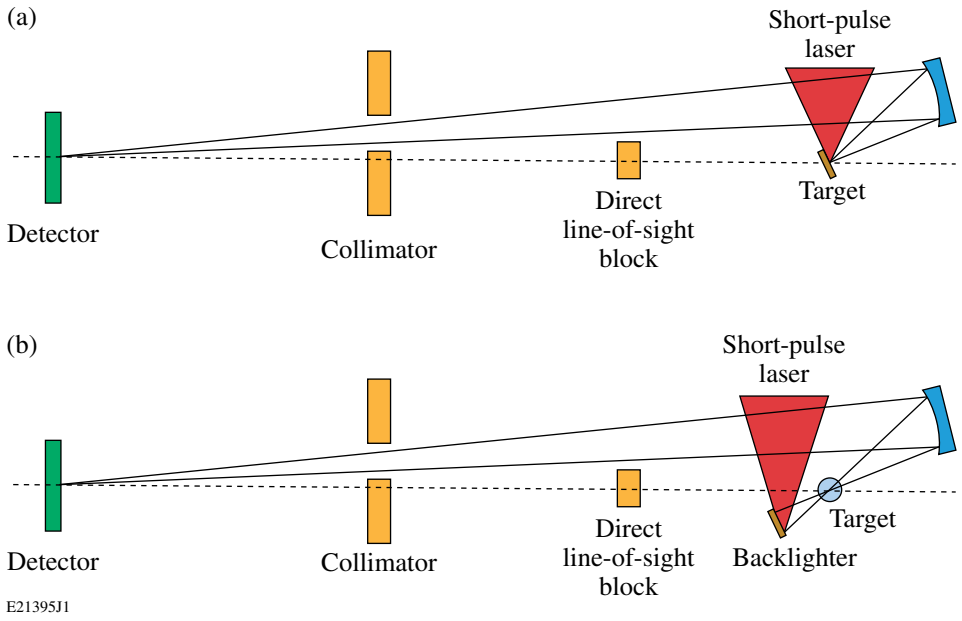

Figure 5.20
Schematic of the spherical crystal imager in (a) self-emission and (b) backlighter mode. The target is placed in the focal plane of the spherical imager. The laser irradiates either (a), the primary target, which emits x rays that are imaged onto the detector or (b) a secondary backlighter target that generates x rays that are absorbed by the primary target, which might be heated by a second laser system (not shown here). Multiple high-Z collimators as well as a line-of-sight block are used to optimize the signal-to-background ratio of the imaging systems.

to reflect the Cu K_α line at ~8 keV with a Bragg angle of 88.7°, or along the 1011 planes to reflect the Si He_α line at ~1.865 keV with a Bragg angle of 83.9°. In an effort to optimize the signal-to-background ratio of the imaging systems, multiple tungsten collimators as well as a line-of-sight block (see Fig. 5.20) are deployed on all SCI systems at LLE.

5.7 SOFT X-RAY POWER DIAGNOSTICS

5.7.1 Dante

Dante is a time-resolved x-ray spectrometer developed by LLNL and used on the Nova and OMEGA lasers.[93,94] This diagnostic measures the soft-x-ray power in a number of channels defined by the combination of filter edges. The detectors are planar vacuum x-ray diodes with Al, Ni, or Cr cathodes. High-speed (5 GHz) digitizers are used to time resolve the signals. The primary function of Dante is to measure the absolute, spectrally resolved, radiation flux from a hohlraum. The version of Dante installed on OMEGA has a total of 18 channels with nominal energies ranging from ~60 eV to ~15 keV. Precision calibration has been carried out using two beamlines [U3C (50 eV to 1 keV) and X8A (1 to 6 keV)] at the National Synchrotron Light Source.

5.7.2 DMX

DMX[95] was developed by CEA as an x-ray spectrometer for eventual use on the NIF and LMJ.[96] It has 18 energy channels ranging from 50 eV to 20 keV. The softer bands (<1.5 keV) use a combination of mirrors and filters and a coaxial diode detector. The mirror/filter combination is designed to improve hard x-ray rejection. The intermediate channels (from 1.5 keV to 5 keV) use only a filter and a coaxial diode. The highest-energy channels use a photoconductive detector (neutron-damaged GaAs) instead of an x-ray diode detector. The absolute x-ray response of the diodes and the relative transmissions of the mirror/filter combinations have been calibrated on a synchrotron beamline at the Laboratoire pour l'Utilisation du Rayonnement Electromagnetique in Orsay. DMX has been used for several hohlraum physics campaigns on OMEGA.

5.8 VELOCITY INTERFEROMETRY SYSTEM FOR ANY REFLECTOR (VISAR) AND ACTIVE SHOCK BREAKOUT (ASBO)

The velocity interferometry system for any reflector (VISAR) diagnostic[97] is available on both OMEGA and OMEGA EP. It detects the Doppler shift of a probe beam reflected off a moving surface, which may be a shock in a transparent medium or the rear target surface. Equation-of-state and shock-timing experiments use this diagnostic. LLE is responsible for this diagnostic and optimized it to operate as a routine facility diagnostic.

The VISAR system (Fig. 5.21) comprises four primary components: a probe laser, an imaging system, two Mach–Zehnder interferometers, and two ROSS streak cameras. The probe laser is a custom Agilite from Continuum.[98] This is a frequency-doubled Nd:YAG laser that produces 50-ns and 100-ns pulses at 5 Hz.

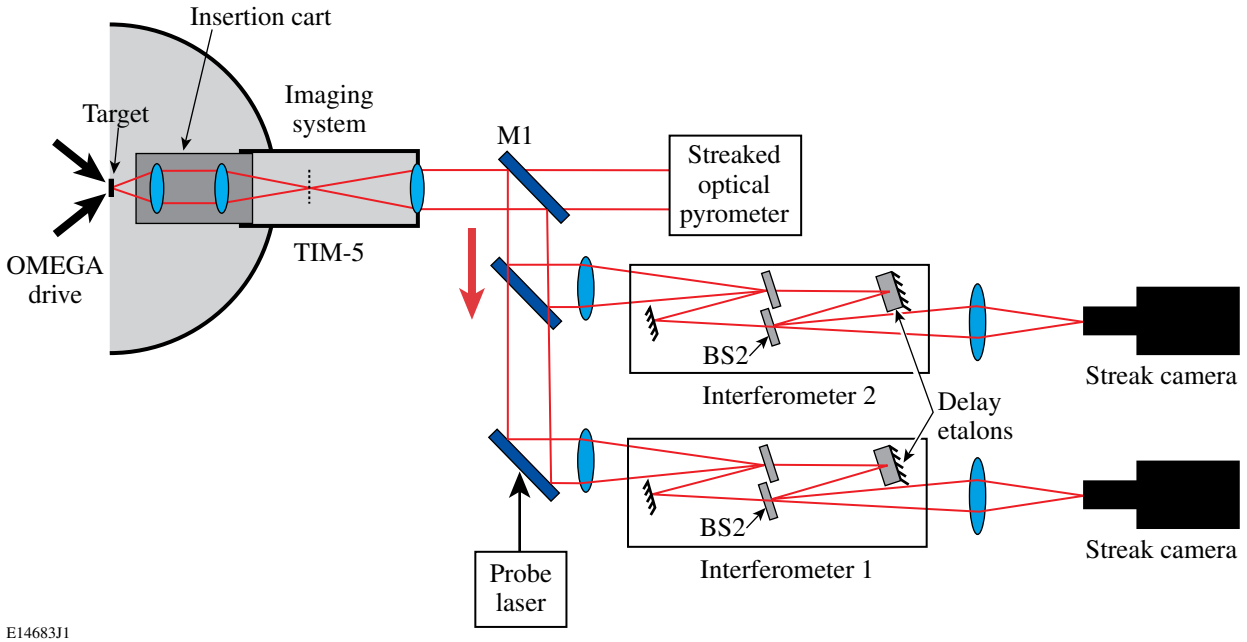

Figure 5.21
Schematic of VISAR diagnostic system.

The probe laser is fiber-optically coupled to the rest of the VISAR system. The imaging system relays an image of the rear target surface to the interferometers' output beamsplitters (BS2). It also conveys the probe beam to and from the target. Each interferometer has an optical etalon (delay) in one leg, providing a comparison of the phases of the reflected probe beam signal at two different times. The result is a series of fringes (imposed onto the target image) whose displacements are proportional to the velocity of the rear surface, resolved in space along the face of the target transverse to the direction of shock propagation. These fringe patterns are detected with an optical streak camera to provide a record of velocity as a function of space and time, with ~5-μm spatial resolution and ~10- to 50-ps temporal resolution, depending on the sweep speed. The second channel has a different velocity sensitivity to resolve the 2$\mathbf{r}$ ambiguities that result when instantaneous velocity jumps (from shocks) are greater than one fringe period.

The detection of the shock-breakout time from opaque samples is possible with VISAR by simply monitoring the rear surface of the target. When the diagnostic is run in this mode, it is referred to as active shock breakout (ASBO). If the shock is weak, it will initiate movement of the surface that will be detected by VISAR. If the shock is strong, it will vaporize the surface and the expanding material will absorb the VISAR probe beam. In either case the arrival time of the shock is measured. The coating on the periscope mirror (M1) is designed to transmit the self-emission from the target to the streaked optical pyrometer, allowing simultaneous velocity and temperature measurements.

Two significant upgrades to this system have recently been implemented. The system now includes new ROSS streak cameras and an entirely new optical system installed to facilitate rapid

installation and streamline operation. The new system has excellent performance and has decreased the diagnostic preparation time required for each shot.

A measure of the precision of the VISAR diagnostic is the correlation of the velocities deduced from the two channels. Figure 5.22 shows the velocity profiles recorded on an isentropic compression experiment that produces a slow, continuous target compression. This results in a rear-side velocity that increases over many nanoseconds. The excellent agreement between the two channels and its persistence for over 10 ns demonstrates the accuracy and stability of the system.

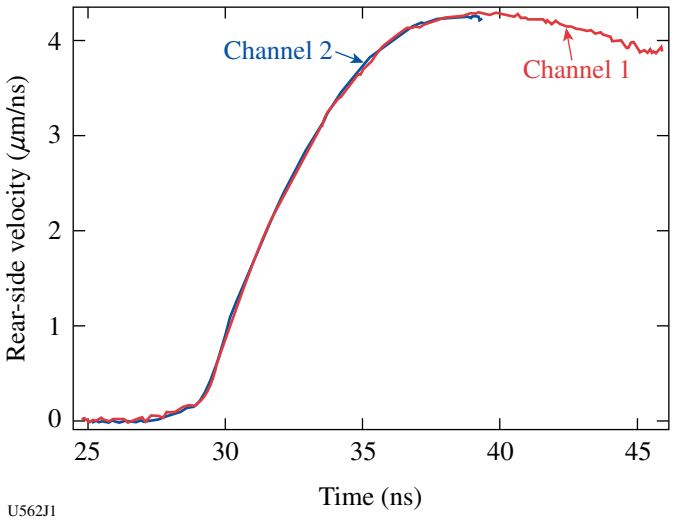

Figure 5.22
Rear-side velocity from an isentropically compressed target measured by two VISAR channels.

5.9 STREAKED OPTICAL PYROMETER

Shocks driven by laser-produced plasmas on OMEGA typically have temperatures greater than 5000 K and produce optical emission. This emission is measured by streaked optical pyrometer (SOP),[99] which uses the VISAR telescope and an optical relay (optimized for 650-nm light) coupled to an optical ROSS streak camera. This system has been modified so that it can be used simultaneously with the VISAR system (Sec. 5.8). Referring to Fig. 5.23, the self-emission light in the 590- to 850-nm range leaks through one of the periscope mirrors (M1) and enters the streaked optical pyrometer. Correction optics compensate for the refractive VISAR telescope used at these wavelengths. The result is a system that provides simultaneous velocity (VISAR) and temperature measurements (streaked optical pyrometer) and has been extremely useful for equation-of-state and shock-timing experiments.

The optical relay was upgraded in 2012 and optimized for 650 nm. The new optical system (Fig. 5.24) has an image relay (three lenses), six mirrors, a Dove prism (for image rotation), and a filter box for attenuating signal. This system has increased the sensitivity by a factor of 6 and enabled the detection of wavelengths from 590 nm to 850 nm. The higher sensitivity allows for a better detection of phase-transition (melt) signals, and the multiple wavelengths allow for color-temperature measurements.

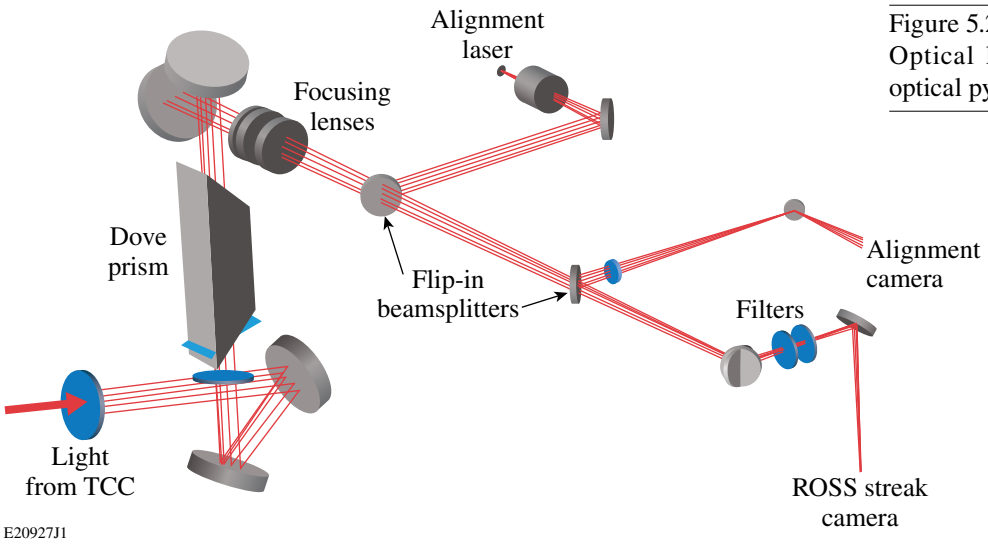

Figure 5.23
Optical layout of the streaked optical pyrometer.

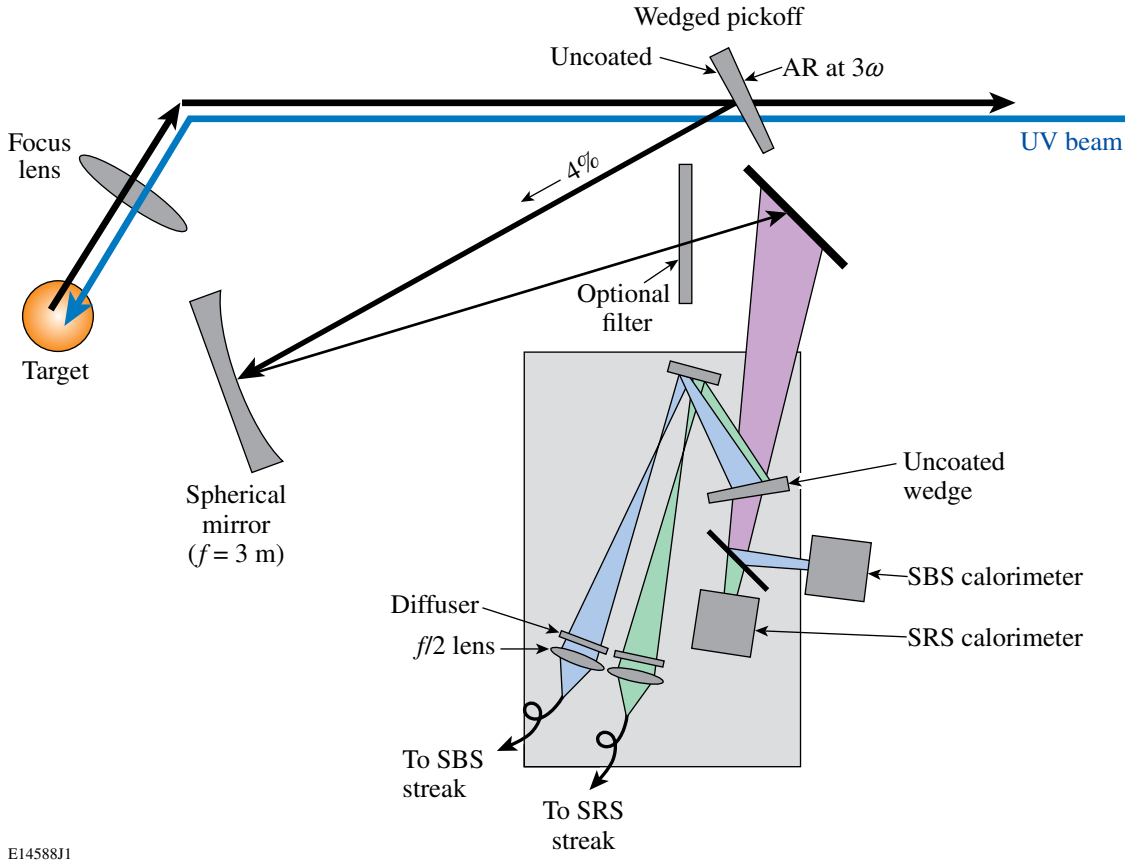

Figure 5.24
Layout of one of the full-aperture backscatter stations (FABS). Light scattered by the target is collected by the focus lens of one of the OMEGA beams. A planar reflection from an uncoated surface of a glass wedge directs 4% of the scattered light to calorimeters and fibers connected to spectrometers and streak cameras for the analysis of stimulated Brillouin scattering (SBS, around 351 nm) and stimulated Raman scattering (SRS, between 400 and 700 nm).

The responsivity of the pyrometer has been calibrated using a lamp whose calibration is traceable to a National Institute of Standards and Technologies standard. The lamp is placed in the OMEGA target chamber and viewed with a standard experimental configuration. Various narrowband filters are inserted to measure the spectral response. An initial guess for the system response was taken as the product of the published spectral response of the S20 photocathode and the measured transmission spectra of the wavelength-dependent optical elements. The spectral response curve was then adjusted to reproduce the spectroscopic measurements. For a Planckian source, this provides a relatively simple relation between the recorded signal and the brightness temperature of the body. The constants used to adjust the spectral response are updated to follow optical element changes and system degradation and are available for each experiment.

5.10 THOMSON SCATTERING

Thomson scattering is a routine diagnostic in high-energy-density laser-plasma experiments[100,101] for characterizing the electron density, and electron and ion temperatures by spectrally resolving light scattered from electron plasma and/or ion-acoustic waves. The Thomson-scattering system on OMEGA uses an optical probe beam ($\lambda_{2\omega}$ = 527 nm or $\lambda_{4\omega}$ = 263 nm) (Ref. 102) and a broadband (190-nm to 850-nm) high-efficiency imaging system to characterize the light scattered from a plasma.[103] There are two main operational modes for the system (1) streaked Thomson scattering and (2) imaging Thomson scattering. Streaked Thomson scattering spectrally and temporally resolves light scattered from a small, ~50 × 50 × 50-μm^3 volume (Thomson-scattering volume). Imaging Thomson scattering spectrally and spatially (along the Thomson-scattering probe-beam axis) resolves light scattered from a ~50 × 50 × 1000-mm^3 volume (Ref. 104). The Thomson-scattering system can also be used for experimental configurations, which do not include the use of the B25 probe beam. In this mode, the system is configured to analyze light scattered from various laser–plasma interactions, such as 3/2ω, ω/2, SBS, etc.

5.10.1 Optical Probes

The Thomson-scattering probe beam is derived from the existing beamline 25 on the OMEGA Laser. When the facility is configured for Thomson-scattering operations, Beam 25 is diverted to Port 9 and no 3ω light is available to target from B25. The Beam 25, third-harmonic frequency generator is detuned to allow for a maximum of 400 J of 2ω ($\lambda_{2\omega}$ = 527 nm) light in a 1-ns square pulse (Table 5.6) to propagate to the target chamber via three 2ω transport mirrors. After reflecting from the last turning mirror, the light propagates through a frequency quadrupler providing up to 200 J of 4ω light to be generated in a 1-ns square pulse. A focusing lens (*f*/6.7) in Port 9 is used to produce a 40±10-μm FWHM best-focus laser spot.[102]

Table 5.6: Standard Thomson-scattering beam parameters.

	Maximum Energy (100-ps long pulse)	Maximum Energy (1-ns long pulse)
2ω probe		400 J
4ω probe		200 J

The pulse shape for the Thomson-scattering probe is determined by the driver feeding the LEG2 beams. Typically, when a short-pulse Thomson-scattering probe is required (e.g., for imaging Thomson scattering), LEG2 is fed by a 100-ps FWHM pulse. The relative timing of the Thomson-scattering probe to the other beams is maintained using the PLAS and/or the driver delays. The PLAS delay limits the maximum beam-timing difference to 4 ns. If beam timings greater than 4 ns are required, beams outside of LEG2 must be used with a driver delay.

5.10.2 Scattered-Light Diagnostic

A reflective optical-transport system is implemented on the OMEGA Thomson-scattering system that enables one to diagnose light from 190 nm to 850 nm (Ref. 103). The spectral range is limited by air attenuation in the UV and photocathode sensitivity in the IR. The system consists of a reflective telescope mounted in a ten-inch manipulator (TIM) that collects scattered light and directs it along the TIM-6 line of sight to an instrument cart located approximately 8 m away from the target. A set of Pfund telescopes focus the scattered light into three independently configurable target diagnostics (ion-acoustic wave, electron plasma wave, and two-plasmon decay imager). The system collects light within *f*/10 cones along the vector defined in the OMEGA coordinate system (θ, ϕ). The optical system is capable of resolving ~15 μm in the plasma plane.

The image of the plasma is rotated so that the P9 (Thomson-scattering probe) axis is vertical on the diagnostic tables and a variable periscope in the transport provides a ±10° range around this axis.[105] In practice, this makes it possible for the Thomson-scattering probe beam to be aligned with the spectrometer slits for imaging Thomson-scattering measurements.

5.10.2.1 Ion-acoustic wave (IAW)

The ion-acoustic wave diagnostic typically uses an *f*/20 focusing mirror to form an image of the plasma at the entrance plane of the 1-m (*f*/9) Czerny–Turner spectrometer. Several pinhole/slit options for defining the Thomson-scattering volume are available. An optical streak camera (S-20 ROSS) and gated CCD camera (PiMax-3 with a Gen II intensifier) are coupled to the exit of the spectrometer (an internal mirror in the spectrometer determines the detector to be used on a particular experiment).

The sweep speed on the optical streak cameras are selectable to provide a 1.5-ns, 5-ns, 15-ns, and 25-ns window. The temporal resolution is typically dominated by the pulse-front introduced by the spectrometer and is of the order of 100 ps when using a 3600-ll/mm grating.[106]

The point-spread function for the Pi-Max3 cameras was measured to have a 40-mm FWHM. The end-to-end spatial resolution measured using a 4-μm-core, single-mode fiber optic positioned at TCC is 20 μm (Ref. 105). The field-of-view along the P9 axis is 800 μm. The minimum gate exposure duration for the camera is 3 ns (Table 5.7).

Table 5.7: Currently available grating options for the IAW system.*

IAW Gratings	Spectral Range	Spectral Window	Spectral Resolution*
1800 ll/mm	190 nm to 850 nm	7 nm	0.05 nm
2400 ll/mm	190 nm to 850 nm	6 nm	0.04 nm
3600 ll/mm	190 nm to 450 nm	3.5 nm	0.025 nm
*Assumes a slit width of 100 μm.			

5.10.2.2 Electron-plasma wave (EPW)

The electron-plasma wave diagnostic typically uses an *f*/20 focusing mirror to form an image of the plasma at the entrance plane of the 0.3-m (*f*/5) Czerny–Turner spectrometer. Several pinhole/ slit options for defining the Thomson-scattering volume are available. An optical streak camera (S-20 ROSS) and gated CCD camera (PiMax-3 with a Gen II intensifier) are coupled to the exit of the spectrometer (an internal mirror in the spectrometer determines the detector to be used on a particular experiment).

The sweep speed on the optical streak cameras is selectable to provide a 1.5-ns, 5-ns, 15-ns, and 25-ns window.

The point-spread unction for the Pi-Max3 cameras was measured to have a 40-mm FWHM. The end-to-end spatial resolution measured using a 4-μm-core, single-mode fiber optic positioned at TCC is 20 μm (Ref. 105). The field-of-view along the P9 axis is 2 mm. Minimum gate exposure duration for the camera is 3 ns (Table 5.8).

Table 5.8: Currently available grating options for the EPW system.*

EPW Gratings	Spectral Range	Spectral Window	Spectral Resolution*
300 ll/mm	190 nm to 850 nm	160 nm	0.12 nm
600 ll/mm	190 nm to 850 nm	80 nm	0.6 nm
1200 ll/mm	190 nm to850 nm	40 nm	0.3 nm
* Assumes a slit width of 100 μm.			

5.10.2.3 2-D imager (TPDI)

A gated CCD camera (PiMax3 with a Gen II intensifier) is used to obtain a 2-D image of the light scattered from the plasma. Several bandpass filters are available. This system has a magnification of 3.2× providing a 2-mm × 2-mm field-of-view with a spatial resolution of 20 μm. The minimum gate exposure duration for the camera is 3 ns.

5.11 FULL-APERTURE BACKSCATTER STATIONS

Two full-aperture backscatter stations (FABS) are routinely operated on OMEGA. These stations are used to characterize the light backscattered from the target through focusing lenses. The information obtained from these stations is critical for understanding laser–plasma interaction experiments[107,108] and interpreting target-implosion experiments and is required for detailed comparisons with code simulations.

The FABS (Fig. 5.25) measures backscattered light energies and temporally resolved spectra in the regions of stimulated Raman scattering (SRS, λ = 400 to 700 nm) and stimulated Brillouin scattering (SBS, λ = 351 nm). All of the light collected by the focus lenses of beams 25 and 30 is diagnosed, as is 351-nm light sampled from the H13 and H17 diagnostic ports. The instruments in the FABS were designed and implemented in collaboration with LLNL.

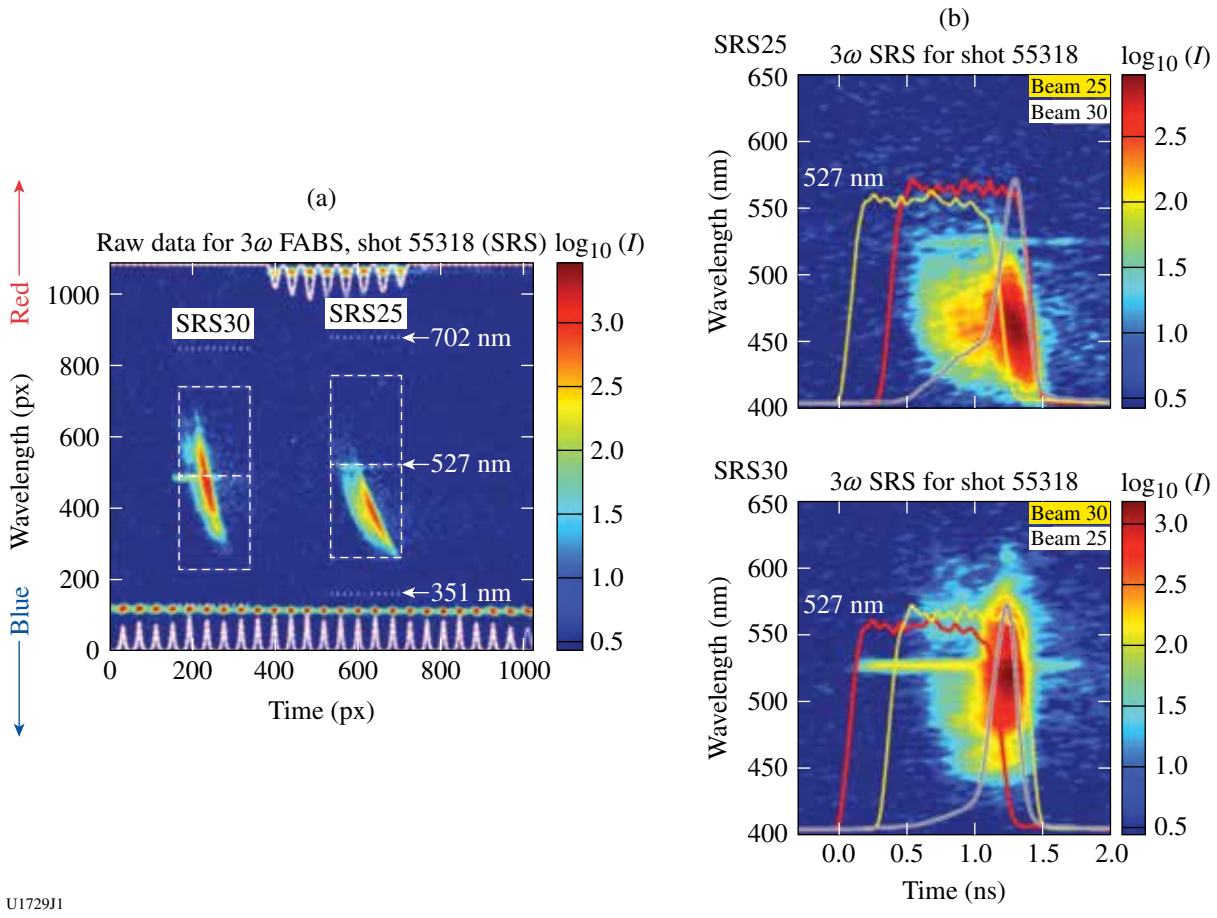

Figure 5.25
(a) Multiplexed SRS streak-camera record for an OMEGA shot. (b) Detailed reductions of the SRS records for FABS25 and FABS30. The data are corrected for group-velocity dispersion in the 10-m optical fiber between the FABS stations and the spectrometer.

The SBS (351-nm) calorimeters have been cross-calibrated with a through-the-tank shot at low beam energy and with a large-aperture reference calorimeter placed behind the wedged pickoff in Fig. 5.25. The SRS (400- to 700-nm) calorimeters have been calibrated using measured electrical calibration constants for the calorimeters and measured transmission and reflection coefficients for all optical components between the calorimeters and the target. Typical energy measurements with the SRS calorimeters have uncertainties of 5% to 10%. For large energy reflections from the target, an optional neutral density filter protects the optical components of the FABS.

The temporally resolved SBS and SRS data are coupled into 435-μm-diam, gradient-index light fibers using *f*/2 lenses and holographic diffusers, as shown in Fig. 5.25. The fibers are ~10 m long and are coupled into two spectrometer-streak-camera systems, one each for SRS and SBS. The SBS and SRS signals from FABS25 and FABS30 are time multiplexed onto two high-performance S20 ROSS streak systems. Channels are also space multiplexed in the SBS system to include the H13 and H17 signals.

A group-velocity correction is applied to the SRS spectra since the blue part of the spectrum arrives ~3 ns after the red part. This correction can be seen by comparing the images in Fig. 5.26. No such correction is required for the SBS spectra. The spectral and temporal resolutions are $\Delta\lambda$ ~ 0.04 nm and Δt ~ 80 ps for SBS, and $\Delta\lambda$ ~ 9 nm and Δt ~ 100 ps for SRS.

A fiducial comb consisting of eight 527-nm pulses spaced at 548 ps is simultaneously added to the streak camera photocathode to allow absolute timing of the scattered-light spectra relative to the main laser pulse. A 2-GHz comb generated by the ROSS system is also injected to calibrate the time axis for both the SBS and SRS systems.

Typical data obtained with the SBS channel for a spherical implosion has been discussed in the literature.[109] As shown in Fig. 5.26, a fourth channel has been added since the sited discussion. The raw, multiplexed data are shown in Fig. 5.26(a) and separate single-channel analyses are shown in Fig. 5.26(b). A scattered component at the laser wavelength (λ_L = 351 nm) is seen through the focus lenses (SBS25 and SBS30) but not the H13 or H17 diagnostic ports and is due to light transmitted past the target ("blow-by"). The time-resolved data are cross-calibrated with the time-integrated scattered-light calorimeter measurements for FABS25 and FABS30. Streaked data such as that presented here allow for quantitative analysis and comparison with hydrodynamic simulations; for example, the time-varying blue shift seen here provides information on the rate of expansion of the coronal plasma. While the data of Fig. 5.26 show no obvious evidence for SBS, many long-scale-length plasma experiments in planar geometry have provided clear evidence of SBS.

Similar multiplexed time-resolved spectral data (Fig. 5.25) are obtained for the two SRS channels. The reduced data is shown in Fig. 5.25(b).

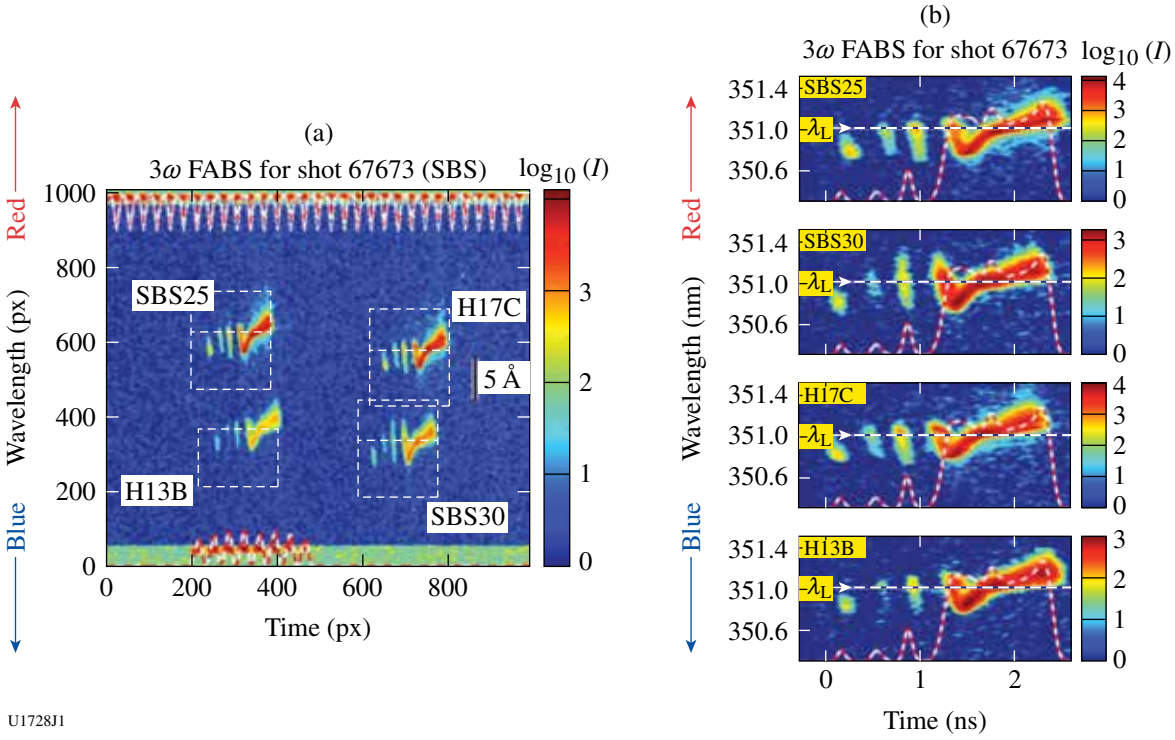

Figure 5.26
(a) Multiplexed temporally and spectrally resolved records of scattered light from a spherical target implosion on OMEGA (shot 67673). Two channels correspond to scattered-light measurements through the focus lenses of beams 25 and 30 and H13B and H17C shows light observed between the focusing lenses through the hex diagnostic ports H13 and H17. The signal intensity (I) is displayed on a logarithmic scale, and the time scale is calibrated using a series of fiducial pulses with a separation of 548 ps and the 2-GHz comb. (b) Analysis of the individual channels, along with the incident laser pulse measured for beam 40 (red-and-white dashed lines) on a linear scale.

5.12 NEAR-BACKSCATTER IMAGING

Two cameras have been installed on OMEGA for the purpose of near-backscatter imaging (NBI). The cameras are designed to measure light scattered by the target into the vicinity of the focus lenses of beams 25 and 30. This light may be 351-nm light reflected from the target, or it may be the result of nonlinear processes such as stimulated Brillouin scattering (SBS), stimulated Raman scattering (SRS), or cross-beam energy transfer. This light is not measured by the full-aperture backscatter station (FABS, Sec. 5.11).

The physical layout of the NBI system is shown in Fig. 5.27. It is similar to the NBI system implemented on Nova.[110] In some circumstances, laser light scattered by the target is directed back toward the laser but extends beyond the incident beam aperture and strikes a scatter plate surrounding the focus lens. Light reflected off the scatter plate is imaged onto two time-integrating cameras, one (SBS-NBI) filtered for 351±10 nm and the other (SRS-NBI) filtered for 400 to 710 nm. The cameras are operated in air inside re-entrant tubes in the OMEGA target chamber.

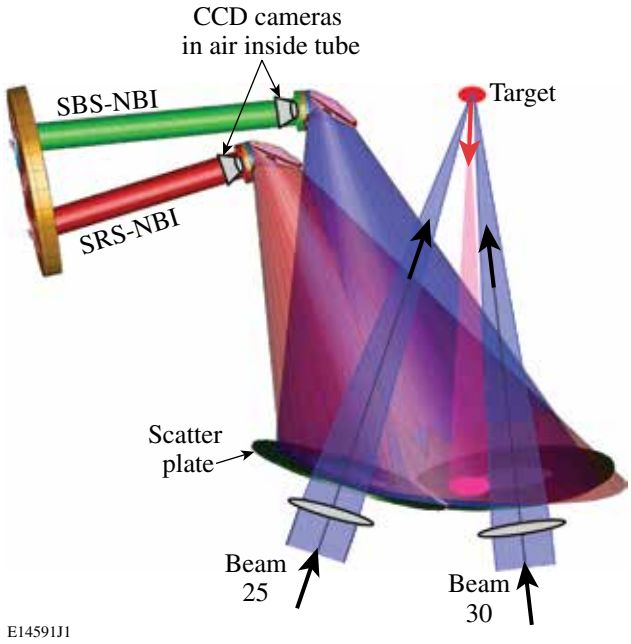

Figure 5.27
Experimental layout of the SBS and SRS near-backscatter-imaging (NBI) channels in the OMEGA target chamber. Bead-blasted aluminum scatter plates surround beams 25 and 30, which pass unimpeded through the central holes in the plates. A directed backscatter beam is shown schematically in pink, striking the scatter plate outside the central hole. The two NBI cameras, filtered for SBS and SRS, photograph the time-integrated image of the scattered light from the scatter plates. The cameras are located in air inside re-entrant tubes.

A typical raw CCD image is shown in Fig. 5.28(a). This shows a highly directed beam of scattered light, a fraction of which is diagnosed by the FABS. To provide a quantitative analysis [Fig. 5.28(b)], the images of each scatter plate are corrected for geometrical distortion as the oblique observation angle and varying image distances cause significant magnification changes across the image of each plate. The flat-fielding analysis also incorporates appropriate corrections for the angles

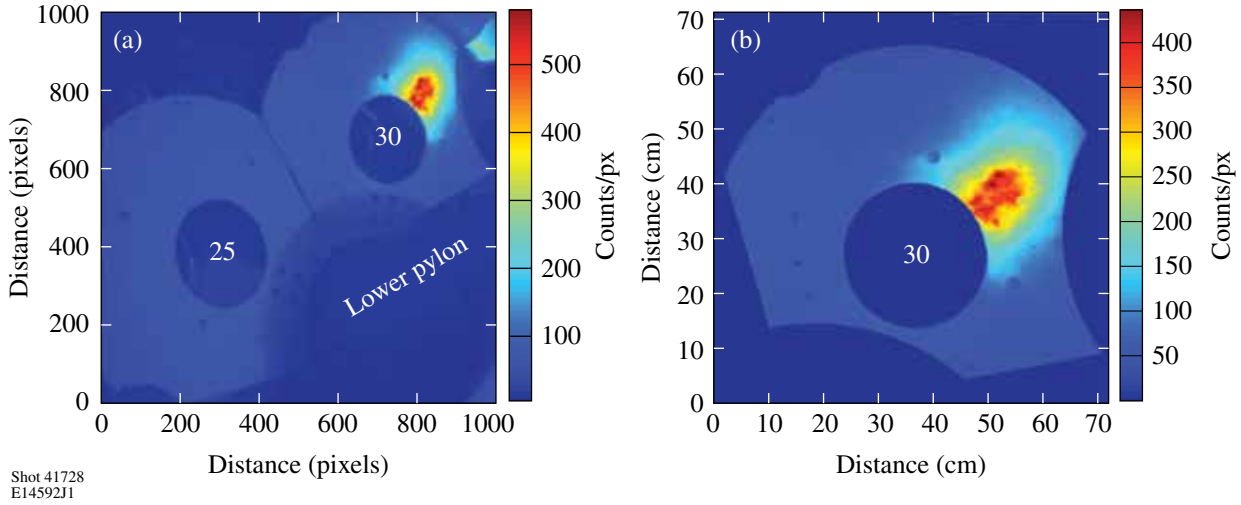

Figure 5.28
NBI images from the SBS channel for OMEGA shot 41728. (a) Raw image with geometrical image distortion due to the oblique viewing angle. (b) Image of the beam-30 NBI plate corrected for geometrical image distortion. Cut-outs and shadowed regions of the scatter plates are blocked out in (b).

of incidence and observation at each point on the scatter plates. Since the field of view of the camera extends to angles well beyond 10° from the optical axis, additional flat-field corrections must be applied. Previously, the scatter plates were painted to provide a near Lambertian scattering source. However, due to target debris coating the plates in a short period of time, the painted scatter plates have been replaced with the original style bead-blasted Al plates. While this makes quantitative analysis problematic, the longer term reproducibility of the data is expected to improve. Further development of the analysis of the NBI images is in progress.

5.13 4ω PROBE DIAGNOSTIC

A 10-ps, 4ω (263-nm), 20-mJ probe beam has been activated on OMEGA EP along with an associated *f*/4 collection diagnostic capable of imaging 5-μm features over a 3.7-mm field-of-view at target chamber center.[111] This system provides a unique capability to diagnose and characterize spatial density structures in a wide variety of plasmas. The diagnostic is designed to characterize long-scale-length plasmas over a field of view that is several millimeters in diameter and to detect localized channels with high spatial and temporal resolution.

5.13.1 Optical Transport and Diagnostic Table

The probe beam slowly diverges through TCC at *f*/25 and is relay imaged over 4 m to a diagnostic table. The catadiaptric collection optics along with a narrow bandpass filter provide many orders of magnitude of rejection between the 4ω probe and the 1ω and 3ω drive beams. The bandpass filter additionally provides rejection of thermal radiation outside of a 2-nm bandwidth centered around 263 nm.

Once on the diagnostic table, the probe beam is split into three legs, as seen in Fig. 5.29. Each leg forms an image of the plasma plane on a 16-bit PIXIS CCD camera that has a 2048 × 2048 window with a pixel size of 13.5 μm.

5.13.2 Angular Filter Refractometry/Shadowgraphy

The first two legs are identical and can be used for angular filter refractometry (AFR[112]) or shadowgraphy. In the presence of a plasma, or some other refractive and/or opaque object, the image on the camera corresponds to a shadowgraph.

The AFR diagnostic uses an angular filter (see Fig. 5.29) placed at the focus of the unrefracted probe beam before coming to the final imaging lens. In this plane, the spatial location of the probe rays is directly proportional to the amount of refraction experienced at TCC. The opaque regions of the angular filter block bands of refraction angles, resulting in shadows in the image plane. The plasma density can be calculated from the measured refraction angles. A detailed description of this diagnostic can be found in Ref. 112. The system has been calibrated using a negative lens at TCC, resulting in a relation between the radial location of a probe ray at the filter plane, *r,* and the amount of refraction experienced at TCC, θ,

$$\Theta^\circ = (0.368 \pm 0.003) \cdot r[\text{mm}]. \tag{5.13.1}$$

The sensitivity of the diagnostic to small angles of refraction is limited by the size of the central block in the filter, currently providing a measure of θ down to 0.092°. The largest refraction angle is limited by the *f*/4 collection, or around 7°. For a millimeter-scale plasma plume produced by the UV beams irradiating a solid target, these limits in refraction angle correspond to a measured plasma density around 3×10^{19} cm^{-3} and 10^{21} cm^{-3}.

5.13.3 Polarimetry

The third arm of the diagnostic is polarimetry. The diagnostic measures the rotation of the probe-beam's polarization after propagating through the plasma. Twin images are formed from the probe laser by splitting the orthogonal polarization components with a Wollaston prism; spatially localized intensity variations between images indicate polarization rotation. Two magnification setups are possible which involve a movement of the final focusing lens, camera placement, and a different Wollaston prism. A variable size iris (see Fig. 5.29) limits the field of view to 3.7 mm and 1 mm for the $M = 3$ and $M = 12$ cases, respectively.

The diagnostic is calibrated by using a half wave plate near TCC to deterministically rotate the change in polarization of the probe. For small rotations (<±10°), the diagnostic responds according to $\Delta I/I = \text{XX}\ \%/^\circ$, where ΔI and I are the difference between and the sum of the two images, respectively. The smallest rotation detectible decreases with increasing spatial size of the rotation, which is limited at a minimum of 0.XX°.

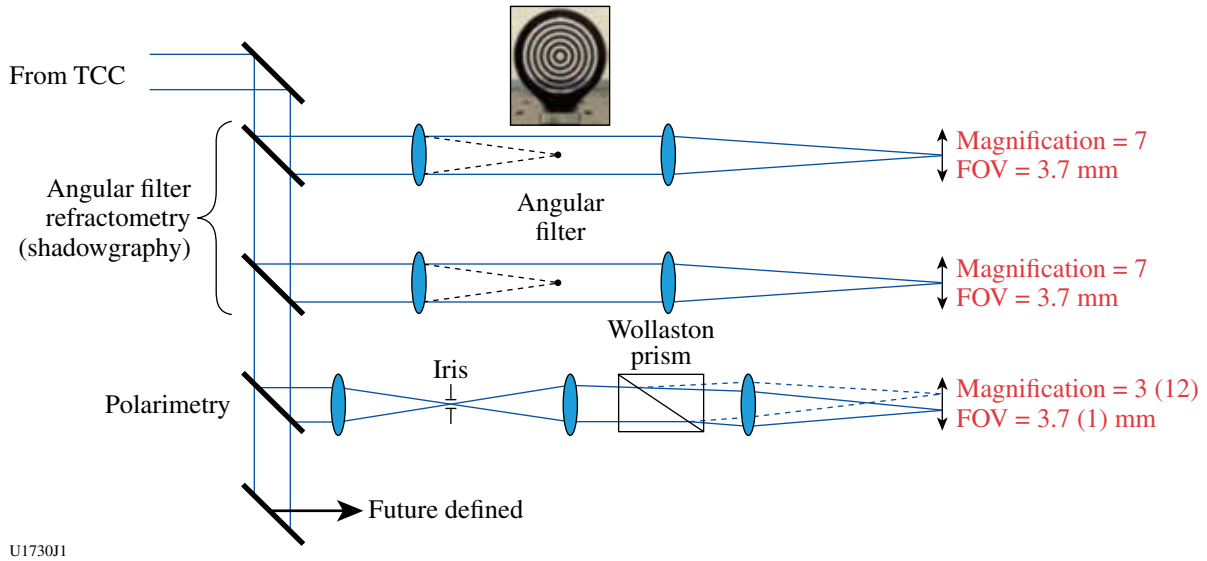

Figure 5.29
The three diagnostic legs of the 4ω probe system.

5.14 MAGNETO-INERTIAL FUSION ELECTRICAL DISCHARGE SYSTEM (MIFEDS)

MIFEDS (magneto-inertial fusion electrical discharge system) is a compact, self-contained pulsed magnetic-field generator. It creates a magnetic field by discharging a capacitor through a small magnetic coil. A detailed description of the system can be found in Ref. 113. A general view of MIFEDS is shown in Fig. 5.30.

The device is enclosed into a TIM-sized aluminum monocoque shroud and contains high-voltage (HV) capacitors charged up to 20 kV with a charging supply. The capacitor is discharged through a small magnetic coil via a spark-gap switch triggered by a trigger pulse generator. The coil (photo insert) is connected to the system by an HV transmission line.

The coil is wound around a plastic coil-form fabricated using 3-D printing technology. This allows for a practically unlimited choice of magnetic-field topology. Some coil shapes used in past experiments are shown in Fig. 5.31. The coils are wound with a Kapton-insulated #24 copper wire with a of 0.030-in. diameter (0.762 mm). Depending on the coil size and number of wire turns, a magnetic field of up to 15 T can be achieved.

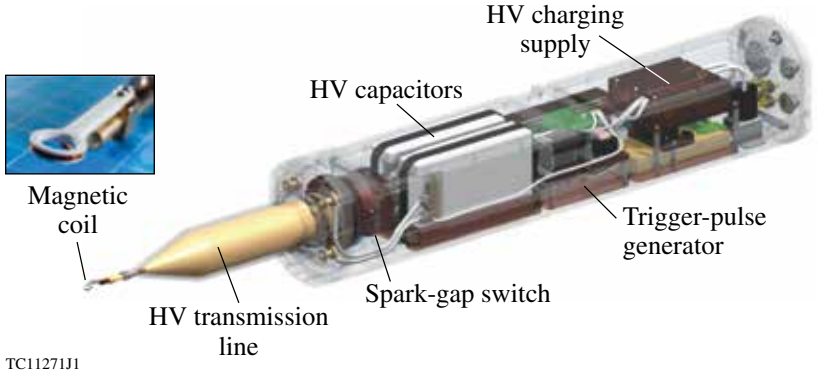

Figure 5.30
MIFEDS general view.

Figure 5.31
A set of different coil shapes.

5.15 EXTERNAL-USER–DEVELOPED DIAGNOSTICS

There are many diagnostic systems available on OMEGA that have been developed by external users, with whom the operational responsibility rests. Some of these diagnostics are listed in Tables 5.9 and 5.10.

Table 5.9: Fixed external-user–developed diagnostics on OMEGA.

Fixed Diagnostic	Institution	Description
Dante	LLNL	Dante is a soft x-ray spectrometer consisting of an array of x-ray diodes in combination with K- and L-shell filters covering energy bands in the range of 50 eV to 20 keV.
Henway X-ray Spectrometer (HXRSP)	LLNL	The HXRSP is a four-channel, time-integrated, film-based x-ray spectrometer covering the range of 1.5 to 13 keV.
Gamma Reaction History Diagnostic (GRH)	LANL	The GRH diagnostic detects 16.7-MeV gamma rays from D–T nuclear reactions by recording their Cherenkov radiation signals from compressed CO_2 or SF6 gas.
Thermoluminescence Dosimeters (TLD)	LLNL	These detectors use small chips of LiF, a material that gives off light when heated after it has been exposed to ionizing radiation. TLD's are fielded in their holder on port H10F to measure radiation produced on OMEGA target shots.

Table 5.10: TIM-based external-user–developed diagnostics on OMEGA.

TIM-Based Diagnostic	Institution	Description
Gas Cherenkov Detectors (GCD)	LANL	Two GCD's are designed to record 16.7-MeV gamma rays from D–T nuclear reactions. The gamma rays interact with the detector's CO_2 fill gas, producing Cherenkov light, which is amplified by a photomultiplier tube and recorded on a stand-alone data-acquisition system.
Gated XR Imager-TRITON (GXI-T)	LANL	The GXI-T is an x-ray framing camera.
Large-Format X-Ray Framing Camera (LFC)	LANL	The LFC is a gated x-ray imaging diagnostic (framing camera) with a 9 × 8-cm image area and six microstrips. Each 680-ps microstrip records up to six images, yielding 36 images in 4 ns of continuous coverage.
Imaging Plate Diagnostic (IPD)	LLNL	The IPD is a static pinhole camera for use with an image plate or standard x-ray film. It features a modified Unimount, compatible with the LLE 12X or any LLNL nose.
OMEGA High Resolution Velocimeter (OHRV)	LLNL	The OHRV is a VISAR capable of capturing velocity nonuniformity modes with wavelengths as short as 2.5 μm.
Powder Diffraction Image Plate 1 (PXRDIP)	LLNL	The PXRDIP acts as both the drive-target mount and diagnostic package for an OMEGA target shot. The configuration allows a sample to be probed with VISAR, while diffracted x rays are simultaneously collected on image plates.
Neutron Imaging System (CEA NIS)	CEA	The CEA NIS records static images, comparable to x-ray pinhole-camera images, of neutron-producing implosion cores.
Neutron Imaging System (LANL NIS)	LANL	The LANL NIS records static images, comparable to x-ray pinhole-camera images, of neutron-producing implosion cores.

5.16 REFERENCES

1. F. H. Séguin, J. A. Frenje, C. K. Li, D. G. Hicks, S. Kurebayashi, J. R. Rygg, B.-E. Schwartz, R. D. Petrasso, S. Roberts, J. M. Soures, D. D. Meyerhofer, T. C. Sangster, J. P. Knauer, C. Sorce, V. Yu. Glebov, C. Stoeckl, T. W. Phillips, R. J. Leeper, K. Fletcher, and S. Padalino, "Spectrometry of Charged Particles from Inertial-Confinement-Fusion Plasmas," Rev. Sci. Instrum. **74**, 975 (2003).

2. M. J. Moran, "Detector Development for γ-Ray Diagnostics of D-T Fusion Reactions," Rev. Sci. Instrum. **56**, 1066 (1985).

3. H. Azechi, M. D. Cable, and R. O. Stapf, "Review of Secondary and Tertiary Reactions, and Neutron Scattering as Diagnostic Techniques for Inertial Confinement Fusion Targets," Laser Part. Beams **9**, 119 (1991).

4. T. E. Blue and D. B. Harris, "The Ratio of D-T and D-D Reactions as a Measure of the Fuel Density-Radius Product in Initially Tritium-Free Inertial Confinement Fusion Targets," Nucl. Sci. Eng. **77**, 463 (1981).

5. H. Azechi, N. Miyanaga, R. O. Stapf, K. Itoga, H. Nakaishi, M. Yamanaka, H. Shiraga, R. Tsuji, S. Ido, K. Nishihara, Y. Izawa, T. Yamanaka, and C. Yamanaka, "Experimental Determination of Fuel Density-Radius Product of Inertial Confinement Fusion Targets Using Secondary Nuclear Fusion Reactions," Appl. Phys. Lett. **49**, 555 (1986).

6. M. D. Cable and S. P. Hatchett, "Neutron Spectra from Inertial Confinement Fusion Targets for Measurement of Fuel Areal Density and Charged Particle Stopping Powers," J. Appl. Phys. **62**, 2233 (1987).

7. S. Kurebayashi, J. A. Frenje, F. H. Séguin, J. R. Rygg, C. K. Li, R. D. Petrasso, V. Yu. Glebov, J. A. Delettrez, T. C. Sangster, D. D. Meyerhofer, C. Stoeckl, J. M. Soures, P. A. Amendt, S. P. Hatchett, and R. E. Turner, "Using Nuclear Data and Monte Carlo Techniques to Study Areal Density and Mix in D_2 Implosions," Phys. Plasmas **12**, 032703 (2005).

8. V. Yu. Glebov, D. D. Meyerhofer, C. Stoeckl, and J. D. Zuegel, "Secondary-Neutron-Yield Measurements by Current-Mode Detectors," Rev. Sci. Instrum. **72**, 824 (2001).

9. S. Skupsky and S. Kacenjar, "Measuring Fuel ρR for Inertial Fusion Experiments Using Neutron Elastic-Scattering Reactions," J. Appl. Phys. **52**, 2608 (1981).

10. H. Nakaishi, N. Miyanaga, H. Azechi, M. Yamanaka, T. Yamanaka, M. Takagi, T. Jitsuno, and S. Nakai, "Fuel Areal Density Measurement of Laser-Imploded Targets by Use of Elastically Scattered Protons," Appl. Phys. Lett. **54**, 1308 (1989).

11. C. K. Li, F. H. Séguin, D. G. Hicks, J. A. Frenje, K. M. Green, S. Kurebayashi, R. D. Petrasso, D. D. Meyerhofer, J. M. Soures, V. Yu. Glebov, R. L. Keck, P. B. Radha, S. Roberts, W. Seka, S. Skupsky, C. Stoeckl, and T. C. Sangster, "Study of Direct-Drive, Deuterium–Tritium Gas-Filled Plastic Capsule Implosions Using Nuclear Diagnostics at OMEGA," Phys. Plasmas **8**, 4902 (2001).

12. D. D. Meyerhofer, J. A. Delettrez, R. Epstein, V. Yu. Glebov, V. N. Goncharov, R. L. Keck, R. L. McCrory, P. W. McKenty, F. J. Marshall, P. B. Radha, S. P. Regan, S. Roberts, W. Seka, S. Skupsky, V. A. Smalyuk, C. Sorce, C. Stoeckl, J. M. Soures, R. P. J. Town, B. Yaakobi, J. D. Zuegel, J. Frenje, C. K. Li, R. D. Petrasso, D. G. Hicks, F. H. Séguin, K. Fletcher, S. Padalino, C. Freeman, N. Izumi, R. Lerche, T. W. Phillips, and T. C. Sangster, "Core Performance and Mix in Direct-Drive Spherical Implosions with High Uniformity," Phys. Plasmas **8**, 2251 (2001).

13. P. B. Radha, S. Skupsky, R. D. Petrasso, and J. M. Soures, "A Novel Charged-Particle Diagnostic for Compression in Inertial Confinement Fusion Targets," Phys. Plasmas **7**, 1531 (2000).

14. J. A. Frenje, C. K. Li, F. H. Séguin, S. Kurebayashi, R. D. Petrasso, J. M. Soures, J. Delettrez, V. Yu. Glebov, D. D. Meyerhofer, P. B. Radha, S. Roberts, T. C. Sangster, S. Skupsky, and C. Stoeckl, "Measurements of Fuel and Shell Areal Densities of OMEGA Capsule Implosions Using Elastically Scattered Protons," Phys. Plasmas **9**, 4719 (2002).

15. D. R. Welch, H. Kislev, and G. H. Miley, "Tertiary Fusion Neutron Diagnostic for Density-Radius Product and Stability of Inertial Confinement Fusion," Rev. Sci. Instrum. **59**, 610 (1988).

16. "Nuclear Diagnostics for High-Density Implosions," *LLE Review Quarterly Report* **69**, 46, Laboratory for Laser Energetics, University of Rochester, Rochester, NY, LLE Document No. DOE/SF/19460-152, NTIS Order No. DE97004432 (1996). Copies may be obtained from the National Technical Information Service, Springfield, VA 22161.

17. R. D. Petrasso, C. K. Li, M. D. Cable, S. M. Pollaine, S. W. Haan, T. P. Bernat, J. D. Kilkenny, S. Cremer, J. P. Knauer, C. P. Verdon, and R. L. Kremens, "Measuring Implosion Symmetry and Core Conditions in the National Ignition Facility," Phys. Rev. Lett. **77**, 2718 (1996).

18. "D-^{3}He Protons as a Diagnostic for Target ρR," *LLE Review Quarterly Report* **73**, 15, Laboratory for Laser Energetics, University of Rochester, Rochester, NY, LLE Document No. DOE/SF/19460-212, NTIS Order No. DE98004497 (1997).

19. C. K. Li, D. G. Hicks, F. H. Séguin, J. A. Frenje, R. D. Petrasso, J. M. Soures, P. B. Radha, V. Yu. Glebov, C. Stoeckl, D. R. Harding, J. P. Knauer, R. L. Kremens, F. J. Marshall, D. D. Meyerhofer, S. Skupsky, S. Roberts, C. Sorce, T. C. Sangster, T. W. Phillips, M. D. Cable,

and R. J. Leeper, "D^3-He Proton Spectra for Diagnosing Shell ρR and Fuel T_i of Imploded Capsules at OMEGA," Phys. Plasmas **7**, 2578 (2000).

20. F. H. Séguin, C. K. Li, J. A. Frenje, S. Kurebayashi, R. D. Petrasso, F. J. Marshall, D. D. Meyerhofer, J. M. Soures, T. C. Sangster, C. Stoeckl, J. A. Delettrez, P. B. Radha, V. A. Smalyuk, and S. Roberts, "Measurements of ρR Asymmetries at Burn Time in Inertial-Confinement-Fusion Capsules," Phys. Plasmas **9**, 3558 (2002).

21. C. K. Li, F. H. Séguin, J. A. Frenje, R. D. Petrasso, R. Rygg, S. Kurebayashi, B. Schwartz, R. L. Keck, J. A. Delettrez, J. M. Soures, P. W. McKenty, V. N. Goncharov, J. P. Knauer, F. J. Marshall, D. D. Meyerhofer, P. B. Radha, S. P. Regan, T. C. Sangster, W. Seka, and C. Stoeckl, "Capsule-Areal-Density Asymmetries Inferred from 14.7-MeV Deuterium–Helium Protons in Direct-Drive OMEGA Implosions," Phys. Plasmas **10**, 1919 (2003).

22. D. G. Hicks, C. K. Li, R. D. Petrasso, F. H. Séguin, B. E. Burke, J. P. Knauer, S. Cremer, R. L. Kremens, M. D. Cable, and T. W. Phillips, "Design of an Electronic Charged Particle Spectrometer to Measure $\langle \rho \mathcal{R} \rangle$ on Inertial Fusion Experiments," Rev. Sci. Instrum. **68**, 589 (1997).

23. D. G. Hicks, "Charged Particle Spectroscopy: A New Window on Inertial Confinement Fusion," Ph.D. thesis, Massachusetts Institute of Technology, 1999.

24. F. H. Séguin, C. K. Li, J. A. Frenje, D. G. Hicks, K. M. Green, S. Kurebayashi, R. D. Petrasso, J. M. Soures, D. D. Meyerhofer, V. Yu. Glebov, P. B. Radha, C. Stoeckl, S. Roberts, C. Sorce, T. C. Sangster, M. D. Cable, K. Fletcher, and S. Padalino, "Using Secondary-Proton Spectra to Study the Compression and Symmetry of Deuterium-Filled Capsules at OMEGA," Phys. Plasmas **9**, 2725 (2002).

25. C. K. Li, F. H. Séguin, J. A. Frenje, S. Kurebayashi, R. D. Petrasso, D. D. Meyerhofer, J. M. Soures, J. A. Delettrez, V. Yu. Glebov, P. B. Radha, F. J. Marshall, S. P. Regan, S. Roberts, T. C. Sangster, and C. Stoeckl, "Effects of Fuel-Shell Mix Upon Direct-Drive, Spherical Implosions on OMEGA," Phys. Rev. Lett. **89**, 165002 (2002).

26. C. K. Li, F. H. Séguin, J. A. Frenje, R. D. Petrasso, J. A. Koch, P. A. Amendt, S. P. Hatchett, S. W. Haan, and N. Izumi, "Using Charged Particles to Measure ρR and ρR Asymmetries for Indirect-Drive Implosions," Bull. Am. Phys. Soc. **48**, 57 (2003).

27. C. K. Li, F. H. Séguin, J. A. Frenje, R. D. Petrasso, J. A. Delettrez, P. W. McKenty, T. C. Sangster, R. L. Keck, J. M. Soures, F. J. Marshall, D. D. Meyerhofer, V. N. Goncharov, J. P. Knauer, P. B. Radha, S. P. Regan, and W. Seka, "Effects of Nonuniform Illumination on Implosion Asymmetry in Direct-Drive Inertial Confinement Fusion," Phys. Rev. Lett. **92**, 205001 (2004).

28. J. A. Frenje, C. K. Li, F. H. Séguin, J. Deciantis, S. Kurebayashi, J. R. Rygg, R. D. Petrasso, J. Delettrez, V. Yu. Glebov, C. Stoeckl, F. J. Marshall, D. D. Meyerhofer, T. C. Sangster, V. A. Smalyuk, and J. M. Soures, "Measuring Shock-Bang Timing and ρR Evolution of D^3He Implosions on OMEGA," Phys. Plasmas **11**, 2798 (2004).

29. C. Stoeckl, V. Yu. Glebov, S. Roberts, T. C. Sangster, R. A. Lerche, R. L. Griffith, and C. Sorce, "Ten-Inch Manipulator-Based Neutron Temporal Diagnostic for Cryogenic Experiments on OMEGA," Rev. Sci. Instrum. **74**, 1713 (2003).

30. R. A. Lerche and R. L. Griffith, "Resolution Limitations and Optimization of the LLNL Streak Camera Focus," in *High Speed Photography, Videography, and Photonics V*, edited by H. C. Johnson (SPIE, Bellingham, WA, 1987), Vol. 832, p. 266.

31. C. Stoeckl, R. E. Bahr, B. Yaakobi, W. Seka, S. P. Regan, R. S. Craxton, J. A. Delettrez, R. W. Short, J. Myatt, A. V. Maximov, and H. Baldis, "Multibeam Effects on Fast-Electron Generation from Two-Plasmon-Decay Instability," Phys. Rev. Lett. **90**, 235002 (2003).

32. W. R. Donaldson, R. Boni, R. L. Keck, and P. A. Jaanimagi, "A Self-Calibrating, Multichannel Streak Camera for Inertial Confinement Fusion Applications," Rev. Sci. Instrum. **73**, 2606 (2002).

33. Goodfellow Corporation, Berwyn, PA 19312-1780.

34. R. A. Lerche, D. W. Phillion, and G. L. Tietbohl, "25 ps Neutron Detector for Measuring ICF-Target Burn History," Rev. Sci. Instrum. **66**, 933 (1995).

35. C. K. Li and R. D. Petrasso, "Charged-Particle Stopping Powers in Inertial Confinement Fusion Plasmas," Phys. Rev. Lett. **70**, 3059 (1993).

36. "Proton Temporal Diagnostic for ICF Experiments on OMEGA," *LLE Review Quarterly Report* **96**, 230, Laboratory for Laser Energetics, University of Rochester, Rochester, NY, LLE Document No. DOE/SF/19460-509, NTIS Order No. PB2006-106668 (2003). Copies may be obtained from the National Technical Information Service, Springfield, VA 22161.

37. S. P. Hatchett, C. G. Brown, T. E. Cowan, E. A. Henry, J. S. Johnson, M. H. Key, J. A. Koch, A. B. Langdon, B. F. Lasinski, R. W. Lee, A. J. MacKinnon, D. M. Pennington, M. D. Perry, T. W. Phillips, M. Roth, T. C. Sangster, M. S. Singh, R. A. Snavely, M. A. Stoyer, S. C. Wilks, and K. Yasuike, "Electron, Photon, and Ion Beams from the Relativistic Interaction of Petawatt Laser Pulses with Solid Targets," Phys. Plasmas **7**, 2076 (2000).

38. L. Gao, P. M. Nilson, I. V. Igumenschev, S. X. Hu, J. R. Davies, C. Stoeckl, M. G. Haines, D. H. Froula, R. Betti, and D. D. Meyerhofer, "Magnetic Field Generation by the Rayleigh-Taylor Instability in Laser-Driven Planar Plastic Targets," Phys. Rev. Lett. **109**, 115001 (2012).

39. M. Borghesi, A. J. Mackinnon, D. H. Campbell, D. G. Hicks, S. Kar, P. K. Patel, D. Price, L. Romagnani, A. Schiavi, and O. Willi, "Multi-MeV Proton Source Investigations in Ultraintense Laser-Foil Interactions," Phys. Rev. Lett. **92**, 055003 (2004).

40. A. Zylstra, C. K. Li, H. G. Rinderknecht, F. H. Séguin, R. D. Petrasso, C. Stoeckl, D. D. Meyerhofer, P. Nilson, T. C. Sangster, S. Le Pape, A. Mackinnon, and P. Patel, "Using High-Intensity Laser-Generated Protons to Radiograph Directly Driven Implosions," Rev. Sci. Instrum. **83**, 013511 (2012).

41. C. Stoeckl, V. Yu. Glebov, J. D. Zuegel, D. D. Meyerhofer, and R. A. Lerche, "Wide-Dynamic-Range 'Neutron Bang Time' Detector on OMEGA," Rev. Sci. Instrum. **73**, 3796 (2002).

42. V. Yu. Glebov, C. Stoeckl, T. C. Sangster, C. Mileham, S. Roberts, and R. A. Lerche, "High-Yield Bang Time Detector for the OMEGA Laser," Rev. Sci. Instrum. **77**, 10E712 (2006).

43. V. Yu. Glebov, C. Stoeckl, T. C. Sangster, S. Roberts, G. J. Schmid, R. A. Lerche, and M. J. Moran, "Prototypes of National Ignition Facility Neutron Time-of-Flight Detectors Tested on OMEGA," Rev. Sci. Instrum. **75**, 3559 (2004).

44. G. J. Schmid, R. L. Griffith, N. Izumi, J. A. Koch, R. A. Lerche, M. J. Moran, T. W. Phillips, R. E. Turner, V. Yu. Glebov, T. C. Sangster, and C. Stoeckl, "CVD Diamond as a High Bandwidth Neutron Detector for Inertial Confinement Fusion Diagnostics," Rev. Sci. Instrum. **74**, 1828 (2003).

45. V. Yu. Glebov, C. Stoeckl, T. C. Sangster, S. Roberts, R. A. Lerche, and G. J. Schmid, "NIF Neutron Bang Time Detector Prototype Test on OMEGA," IEEE Trans. Plasma Sci. **33**, 70 (2005).

46. Tektronix, Inc., Beaverton, OR 97077.

47. H. Brysk, "Fusion Neutron Energies and Spectra," Plasma Phys. **15**, 611 (1973).

48. Harris International, New York, NY 10036.

49. C. Stoeckl, J. A. Delettrez, J. H. Kelly, T. J. Kessler, B. E. Kruschwitz, S. J. Loucks, R. L. McCrory, D. D. Meyerhofer, D. N. Maywar, S. F. B. Morse, J. Myatt, A. L. Rigatti, L. J. Waxer, J. D. Zuegel, and R. B. Stephens, "High-Energy Petawatt Project at the University of Rochester's Laboratory for Laser Energetics," Fusion Sci. Technol. **49**, 367 (2006).

50. V. Yu. Glebov, R. A. Lerche, C. Stoeckl, G. J. Schmid, T. C. Sangster, J. A. Koch, T. W. Phillips, C. Mileham, and S. Roberts, "Progress with CVD Diamond Detectors for ICF Neutron Time-of-Flight Applications," presented at ICOPS 2005, International Conference on Plasma Sciences, Monterey, CA, 20–23 June 2005 (Paper 10281).

51. J. Källne and H. Enge, "Magnetic Proton Recoil Spectrometer for Fusion Plasma Neutrons," Nucl. Instrum. Methods Phys. Res. **A311**, 595 (1992).

52. R. J. Leeper, G. A. Chandler, G. W. Cooper, M. S. Derzon, D. L. Fehl, D. L. Hebron, A. R. Moats, D. D. Noack, J. L. Porter, L. E. Ruggles, J. A. Torres, M. D. Cable, P. M. Bell, C. A. Clower, B. A. Hammel, D. H. Kalantar, V. P. Karpenko, R. L. Kauffman, J. D. Kilkenny, F. D. Lee, R. A. Lerche, B. J. MacGowan, M. J. Moran, M. B. Nelson, W. Olson, T. J. Orzechowski, T. W. Phillips, D. Ress, G. L. Tietbohl, J. E. Trebes, R. J. Bartlett, R. Berggren, S. E. Caldwell, R. E. Chrien, B. H. Failor, J. C. Fernández, A. Hauer, G. Idzorek, R. G. Hockaday, T. J. Murphy, J. Oertel, R. Watt, M. Wilke, D. K. Bradley, J. Knauer, R. D. Petrasso, and C. K. Li, "Target Diagnostic System for the National Ignition Facility," Rev. Sci. Instrum. **68**, 868 (1997).

53. J. Frenje, "Instrumentation for Fusion Neutron Measurements and Experimentation at JET," Ph.D. thesis, Uppsala University, 1998.

54. J. A. Frenje, K. M. Green, D. G. Hicks, C. K. Li, F. H. Séguin, R. D. Petrasso, T. C. Sangster, T. W. Phillips, V. Yu. Glebov, D. D. Meyerhofer, S. Roberts, J. M. Soures, C. Stoeckl, K. Fletcher, S. Padalino, and R. J. Leeper, "A Neutron Spectrometer for Precise Measurements of DT Neutrons from 10 to 18 MeV at OMEGA and the National Ignition Facility," Rev. Sci. Instrum. **72**, 854 (2001).

55. R. Petrasso, Supplemental Proposal to Nuclear Probing of Dense Plasmas—Stewardship Science Academic Alliances Program, Grant #DE-FG03-03NAS00058, request for Purchase of the Magnet for a Magnetic-Recoil Spectrometer for ρR and T_i Measurements of Warm and Cryogenic OMEGA Implosions, and for Warm, Fizzle, and Ignited NIF Implosions, submitted to R. Schneider, U.S. Department of Energy, 24 September 2003.

56. J. A. Frenje, D. T. Casey, C. K. Li, J. R. Rygg, F. H. Séguin, R. D. Petrasso, V. Yu. Glebov, D. D. Meyerhofer, T. C. Sangster, S. Hatchett, S. Haan, C. Cerjan, O. Landen, M. Moran, P. Song, D. C. Wilson, and R. J. Leeper, "First Measurements of the Absolute Neutron Spectrum Using the Magnetic Recoil Spectrometer at OMEGA," Rev. Sci. Instrum. **79**, 10E502 (2008).

57. J. A. Frenje, C. K. Li, F. H. Séguin, D. T. Casey, R. D. Petrasso, T. C. Sangster, R. Betti, V. Yu. Glebov, and D. D. Meyerhofer, "Diagnosing Fuel ρR and ρR Asymmetries in Cryogenic Deuterium-Tritium Implosions Using Charged-Particle Spectrometry at OMEGA," Phys. Plasmas **16**, 042704 (2009).

58. F. J. Marshall, T. Ohki, D. McInnis, Z. Ninkov, and J. Carbone, "Imaging of Laser-Plasma X-Ray Emission with Charge-Injection Devices," Rev. Sci. Instrum. **72**, 713 (2001).

59. F. J. Marshall, J. A. Delettrez, R. Epstein, R. Forties, R. L. Keck, J. H. Kelly, P. W. McKenty, S. P. Regan, and L. J. Waxer, "Direct-Drive-Implosion Experiments with Enhanced Fluence Balance on OMEGA," Phys. Plasmas **11**, 251 (2004).

60. J. Carbone, J. J. Zarnowski, M. Pace, S. Czebiniak, and R. Carta, "Megarad and Scientific CIDs," in *Solid State Arrays and CCD Cameras*, edited by C. N. Anagnostoupoulos, M. M. Blouke, and M. P. Lesser (SPIE, Bellingham, WA, 1996), Vol. 2654, p. 131.

61. F. J. Marshall, T. DeHaas, and V. Yu. Glebov, "Charge-Injection-Device Performance in the High-Energy-Neutron Environment of Laser-Fusion Experiments," Rev. Sci. Instrum. **81**, 10E503 (2010).

62. F. J. Marshall, R. S. Craxton, J. A. Delettrez, D. H. Edgell, L. M. Elasky, R. Epstein, V. Yu. Glebov, V. N. Goncharov, D. R. Harding, R. Janezic, R. L. Keck, J. D. Kilkenny, J. P. Knauer, S. J. Loucks, L. D. Lund, R. L. McCrory, P. W. McKenty, D. D. Meyerhofer, P. B. Radha, S. P. Regan, T. C. Sangster, W. Seka, V. A. Smalyuk, J. M. Soures, C. Stoeckl, S. Skupsky, J. A. Frenje, C. K. Li, R. D. Petrasso, and F. H. Séguin, "Direct-Drive, Cryogenic Target Implosions on OMEGA," Phys. Plasmas **12**, 056302 (2005).

63. D. K. Bradley, P. M. Bell, O. L. Landen, J. D. Kilkenny, and J. Oertel, "Development and Characterization of a Pair of 30–40 ps X-Ray Framing Cameras," Rev. Sci. Instrum. **66**, 716 (1995).

64. J. D. Kilkenny, P. Bell, R. Hanks, G. Power, R. E. Turner, and J. D. Wiedwald, "High-Speed Gated X-Ray Images," Rev. Sci. Instrum. **59**, 1793 (1988).

65. D. K. Bradley, J. Delettrez, P. A. Jaanimagi, F. J. Marshall, C. P. Verdon, J. D. Kilkenny, and P. Bell, "X-Ray Gated Images of Imploding Microballoons," in *High Speed Photography, Videography and Photonics VI*, edited by G. L. Stradling (SPIE, Bellingham, WA, 1988), Vol. 981, p. 176.

66. P. M. Bell, J. D. Kilkenny, G. Power, R. Bonner, and D. K. Bradley, "Multiframe X-Ray Images from a Single Meander Stripline Coated on a Microchannel Plate," in *Ultrahigh Speed and High Speed Photography, Photonics, and Videography VII*, edited by G. L. Stradling (SPIE, Bellingham, WA, 1989), Vol. 1155, p. 430.

67. J. D. Kilkenny, "High Speed Proximity Focused X-Ray Cameras," Laser Part. Beams **9**, 49 (1991).

68. D. K. Bradley, P. M. Bell, J. D. Kilkenny, R. Hanks, O. Landen, P. A. Jaanimagi, P. W. McKenty, and C. P. Verdon, "High-Speed Gated X-Ray Imaging for ICF Target Experiments," Rev. Sci. Instrum. **63**, 4813 (1992).

69. V. A. Smalyuk, T. R. Boehly, L. S. Iwan, T. J. Kessler, J. P. Knauer, F. J. Marshall, D. D. Meyerhofer, C. Stoeckl, B. Yaakobi, and D. K. Bradley, "Fourier-Space Image Processing for Spherical Experiments on OMEGA," Rev. Sci. Instrum. **72**, 635 (2001).

70. M. C. Richardson, R. S. Marjoribanks, S. A. Letzring, J. M. Forsyth, and D. M. Villeneuve, "Spectrally Discriminating Time-Resolved and Space-Resolved X-Ray Plasma Diagnostics," IEEE J. Quantum Electron. **QE-19**, 1861 (1983).

71. F. J. Marshall, J. A. Delettrez, R. Epstein, and B. Yaakobi, "Diagnosis of Laser-Target Implosions by Space-Resolved Continuum Absorption X-Ray Spectroscopy," Phys. Rev. E **49**, 4381 (1994).

72. F. J. Marshall and Q. Su, "Quantitative Measurements with X-Ray Microscopes in Laser-Fusion Experiments," Rev. Sci. Instrum. **66**, 725 (1995).

73. F. J. Marshall and J. A. Oertel, "A Framed Monochromatic X-Ray Microscope for ICF," Rev. Sci. Instrum. **68**, 735 (1997).

74. F. J. Marshall, M. M. Allen, J. P. Knauer, J. A. Oertel, and T. Archuleta, "A High-Resolution X-Ray Microscope for Laser-Driven Planar-Foil Experiments," Phys. Plasmas **5**, 1118 (1998).

75. F. J. Marshall and G. R. Bennett, "A High-Energy X-Ray Microscope for Inertial Confinement Fusion," Rev. Sci. Instrum. **70**, 617 (1999).

76. F. J. Marshall, J. A. Oertel, and P. J. Walsh, "Framed, 16-Image, Kirkpatrick–Baez Microscope for Laser–Plasma X-Ray Emission," Rev. Sci. Instrum. **75**, 4045 (2004).

77. J. Workman, J. R. Fincke, P. Keiter, G. A. Kyrala, T. Pierce, S. Sublett, J. P. Knauer, H. Robey, B. Blue, S. G. Glendinning, and O. L. Landen, "Development of Intense Point X-Ray Sources for Backlighting High Energy Density Experiments (invited)," Rev. Sci. Instrum. **75**, 3915 (2004).

78. D. K. Bradley, O. L. Landen, A. B. Bullock, S. G. Glendinning, and R. E. Turner, "Efficient, 1-100-keV X-Ray Radiography with High Spatial and Temporal Resolution," Opt. Lett. **27**, 134 (2002).

79. C. N. Danson, J. Collier, D. Neely, L. J. Barzanti, A. Damerell, C. B. Edwards, M. H. R. Hutchinson, M. H. Key, P. A. Norreys, D. A. Pepler, I. N. Ross, P. F. Taday, W. T. Toner, M. Trentelman, F. H. Walsh, T. B. Winstone, and R. W. W. Wyatt, "Well Characterized 10^{19} W cm^2 Operation of VULCAN—An Ultra-High Power Nd:Glass Laser," J. Mod. Opt. **45**, 1653 (1998).

80. C. N. Danson, P. A. Brummitt, R. J. Clarke, J. L. Collier, B. Fell, A. J. Frackiewicz, S. Hancock, S. Hawkes, C. Hernandez-Gomez, P. Holligan, M. H. R. Hutchinson, A. Kidd, W. J. Lester, I. O. Musgrave, D. Neely, D. R. Neville, P. A. Norreys, D. A. Pepler, C. J. Reason, W. Shaikh, T. B. Winstone, R. W. W. Wyatt, and B. E. Wyborn, "Vulcan Petawatt—An Ultra-High-Intensity Interaction Facility," Nucl. Fusion **44**, S239 (2004).

81. H.-S. Park, D. M. Chambers, H.-K. Chung, R. J. Clarke, R. Eagleton, E. Giraldez, T. Goldsack, R. Heathcote, N. Izumi, M. H. Key, J. A. King, J. A. Koch, O. L. Landen, A. Nikroo, P. K. Patel, D. F. Price, B. A. Remington, H. F. Robey, R. A. Snavely, D. A. Steinman, R. B. Stephens, C. Stoeckl, M. Storm, M. Tabak, W. Theobald, R. P. J. Town, J. E. Wickersham, and B. B. Zhang, "High-Energy $K\alpha$ Radiography Using High-Intensity, Short-Pulse Lasers," Phys. Plasmas **13**, 056309 (2006).

82. "SPECT3D Imaging & Spectral Analysis Suite, Getting Started," Prism Computational Sciences, Inc., Madison, WI, Report PCS-R-041, Ver. 3.0 (2002).

83. W. Theobald, C. Stoeckl, T. C. Sangster, J. Kuba, R. Snavely, M. H. Key, R. Heathcote, D. Neely, and P. Norreys, "X-Ray Line Emission Spectroscopy of 100-TW Laser-Pulse–Generated Plasmas for Backlighter Development of Cryogenic Implosion Capsules," Bull. Am. Phys. Soc. **49**, 103 (2004).

84. R. G. Evans, E. L. Clark, R. T. Eagleton, A. M. Dunne, R. D. Edwards, W. J. Garbett, T. J. Goldsack, S. James, C. C. Smith, B. R. Thomas, R. Clarke, D. J. Neely, and S. J. Rose, "Rapid Heating of Solid Density Material by a Petawatt Laser," Appl. Phys. Lett. **86**, 191505 (2005).

85. W. Theobald, K. Akli, R. Clarke, J. Delettrez, R. R. Freeman, S. Glenzer, J. Green, G. Gregori, R. Heathcote, N. Izumi, J. A. King, J. A. Koch, J. Kuba, K. Lancaster, A. J. MacKinnon, M. Key, C. Mileham, J. Myatt, D. Neely, P. A. Norreys, H.-S. Park, J. Pasley, P. Patel, S. P. Regan, H. Sawada, R. Shepherd, R. Snavely, R. B. Stephens, C. Stoeckl, M. Storm, B. Zhang, and T. C. Sangster, "Hot Surface Ionic Line Emission and Cold K-Inner Shell Emission from Petawatt-Laser-Irradiated Cu Foil Targets," Phys. Plasmas **13**, 043102 (2006).

86. P. A. Jaanimagi, R. Boni, D. Butler, S. Ghosh, W. R. Donaldson, and R. L. Keck, "The Streak Camera Development Program at LLE," in *26th International Congress on High-Speed Photography and Photonics*, edited by D. L. Paisley, S. Kleinfelder, D. R. Snyder, and B. J. Thompson (SPIE, Bellingham, WA, 2005), Vol. 5580, p. 408.

87. B. L. Henke, J. Liesegang, and S. D. Smith, "Soft-X-Ray-Induced Secondary-Electron Emission from Semiconductors and Insulators: Models and Measurements," Phys. Rev. B **19**, 3004 (1979).

88. PHOTONIS, 19106 Brive, France.

89. Sydor Instruments, LLC, Rochester, NY 14624.

90. P. M. Nilson, S. P. D. Mangles, L. Willingale, M. C. Kaluza, A. G. R. Thomas, M. Tatarakis, Z. Najmudin, R. J. Clarke, K. L. Lancaster, S. Karsch, J. Schreiber, R. G. Evans, A. E. Dangor, and K. Krushelnick, "Generation of Ultrahigh-Velocity Ionizing Shocks with Petawatt-Class Laser Pulses," Phys. Rev. Lett. **103**, 255001 (2009).

91. P. M. Nilson, J. R. Davies, W. Theobald, P. A. Jaanimagi, C. Mileham, R. K. Jungquist, C. Stoeckl, I. A. Begishev, A. A. Solodov, J. F. Myatt, J. D. Zuegel, T. C. Sangster, R. Betti, and D. D. Meyerhofer, "Time-Resolved Measurements of Hot-Electron Equilibration Dynamics in High-Intensity Laser Interactions with Thin-Foil Solid Targets," Phys. Rev. Lett. **108**, 085002 (2012).

92. C. Stoeckl, V. Yu. Glebov, D. D. Meyerhofer, W. Seka, B. Yaakobi, R. P. J. Town, and J. D. Zuegel, "Hard X-Ray Detectors for OMEGA and NIF," Rev. Sci. Instrum. **72**, 1197 (2001).

93. H. N. Kornblum, R. L. Kauffman, and J. A. Smith, "Measurement of 0.1–3-keV X-Rays from Laser Plasmas," Rev. Sci. Instrum. **57**, 2179 (1986).

94. K. M. Campbell, F. A. Weber, E. L. Dewald, S. H. Glenzer, O. L. Landen, R. E. Turner, and P. A. Waide, "OMEGA Dante Soft-X-Ray Power Diagnostic Component Calibration at the National Synchroton Light Source," Rev. Sci. Instrum. **75**, 3768 (2004).

95. J. L. Bourgade, B. Villette, J. L. Bocher, J. Y. Boutin, S. Chiche, N. Dague, D. Gontier, J.-P. Jadaud, B. Savale, R. Wrobel, and R. E. Turner, "DMX: An Absolutely Calibrated Time-Resolved Broadband Soft X-Ray Spectrometer Designed for MJ Class Laser-Produced Plasma (invited)," Rev. Sci. Instrum. **72**, 1173 (2001).

96. M. L. André, "Laser Megajoule Project Status," in *Inertial Fusion Sciences and Applications 99*, edited by C. Labaune, W. J. Hogan, and K. A. Tanaka (Elsevier, Paris, 2000), p. 32.

97. L. M. Barker and R. E. Hollenbach, "Laser Interferometer for Measuring High Velocities of Any Reflecting Surface," J. Appl. Phys. **43**, 4669 (1972).

98. Spectra-Physics, A Division of Newport Corporation, Mountain View, CA 94039.

99. J. A. Oertel, T. J. Murphy, R. R. Berggren, J. Faulkner, R. Schmell, D. Little, T. Archuleta, J. Lopez, J. Verlarde, and R. F. Horton, "Multipurpose 10 in. Manipulator-Based Optical Telescope for OMEGA and the Trident Laser Facility," Rev. Sci. Instrum. **70**, 803 (1999).

100. D. H. Froula, S. H. Glenzer, N. C. Luhmann, and J. Sheffield, *Plasma Scattering of Electromagnetic Radiation: Theory and Measurement Techniques*, 2nd ed. (Academic Press, Burlington, MA, 2011).

101. D. H. Froula, J. S. Ross, L. Divol, N. Meezan, A. J. MacKinnon, R. Wallace, and S. H. Glenzer, "Thomson-Scattering Measurements of High Electron Temperature Hohlraum Plasmas for Laser-Plasma Interaction Studies," Phys. Plasmas **13**, 052704 (2006).

102. A. J. Mackinnon, S. Shiromizu, G. Antonini, J. Auerbach, K. Haney, D. H. Froula, J. Moody, G. Gregori, C. Constantin, C. Sorce, L. Divol, R. L. Griffith, S. Glenzer, J. Satariano, P. K. Whitman, S. N. Locke, E. L. Miller, R. Huff, K. Thorp, W. Armstrong, W. Bahr, W. Seka, G. Pien, J. Mathers, S. Morse, S. Loucks, and S. Stagnitto, "Implementation of a High Energy 4ω Probe Beam on the Omega Laser," Rev. Sci. Instrum. **75**, 3906 (2004).

103. J. Katz, R. Boni, C. Sorce, R. Follett, M. J. Shoup III, and D. H. Froula, "A Reflective Optical Transport System for Ultraviolet Thomson Scattering from Electron Plasma Waves on OMEGA," Rev. Sci. Instrum. **83**, 10E349 (2012).

104. D. H. Froula, J. S. Ross, L. Divol, and S. H. Glenzer, "Thomson-Scattering Techniques to Diagnose Local Electron and Ion Temperatures, Density, and Plasma Wave Amplitudes in Laser Produced Plasmas," Rev. Sci. Instrum. **77**, 10E522 (2006).

105. J. Katz, J. S. Ross, C. Sorce, and D. H. Froula, "A Reflective Image-Rotating Periscope for Spatially Resolved Thomson-Scattering Experiments on OMEGA," J. Instrum. **8**, C12009 (2013).

106. A. Visco, R. P. Drake, D. H. Froula, S. H. Glenzer, and B. B. Pollock, "Temporal Dispersion of a Spectrometer," Rev. Sci. Instrum. **79**, 10F545 (2008).

107. A. J. Martin, R. J. Simms, and R. B. Jacobs, "Beta Energy Driven Uniform Deuterium-Tritium Ice Laser in Reactor-Size Cryogenic Inertial Fusion Targets," J. Vac. Sci. Technol. A **6**, 1885 (1988).

108. W. Seka, R. S. Craxton, R. L. Keck, J. P. Knauer, D. D. Meyerhofer, S. P. Regan, C. Stoeckl, B. Yaakobi, R. E. Bahr, D. Montgomery, H. Baldis, and R. Kirkwood, "Laser-Plasma Interaction Diagnostics for ICF Fusion Research," in *Advanced Diagnostics for Magnetic and Inertial Fusion*, edited by P. E. Stott, A. Wootton, G. Gorini, E. Sindoni, and D. Batani (Kluwer Academic/Plenum Publishers, New York, 2002), p. 27.

109. W. Seka, D. Fried, R. E. Glena, and J. D. B. Featherstone, "Laser Energy Deposition in Dental Hard Tissue," J. Dent. Res. **73**, 340 (1994).

110 R. K. Kirkwood, C. A. Back, M. A. Blain, D. E. Desenne, A. G. Dulieu, S. H. Glenzer, B. J. MacGowan, D. S. Montgomery, and J. D. Moody, "Imaging Backscattered and Near to Backscattered Light in Ignition Scale Plasmas (invited)," Rev. Sci. Instrum. **68**, 636 (1997).

111. D. H. Froula, R. Boni, M. Bedzyk, R. S. Craxton, F. Ehrne, S. Ivancic, R. Jungquist, M. J. Shoup, W. Theobald, D. Weiner, N. L. Kugland, and M. C. Rushford, "Optical Diagnostic Suite (Schlieren, Interferometry, and Grid Image Refractometry) on OMEGA EP Using a 10-ps, 263-nm Probe Beam," Rev. Sci. Instrum. **83**, 10E523 (2012).

112. D. Haberberger, S. Ivancic, S. X. Hu, R. Boni, M. Barczys, R. S. Craxton, and D. H. Froula, "Measurements of the Electron Density Profiles Using an Angular Filter Refractometer," Phys. Plasmas **21**, 056304 (2014).

113. P.-Y. Chang, D. H. Barnak, M. Hohenberger, R. Betti, A. Agliata, W. Bittle, G. Fiksel, D. Hasset, D. Lonobile, M. J. Shoup III, and C. Taylor, "Experimental Platform for Magnetized HEDP Science at OMEGA," Bull. Am. Phys. Soc. **57**, 135 (2012).